RSC Advances

PAPER

View Article Online
View Journal | View Issue

Cite this: *RSC Adv.*, 2025, **15**, 30872

Lysozyme-dequalinium encapsulation in a Zn–Fe LDH–chia seed matrix for enhanced antimicrobial dental therapeutics

Samar M. Mahgoub,[a] Abdullah S. Alawam,[b] Hassan A. Rudayni,[b] Ahmed A. Allam,[b] Sahar Abdel Aleem Abdel Aziz,[c] Abdullah A. Eweis,[d] Esraa Khaled,[e] Rami Shafei,[f] Fatma Mohamed[f] and Rehab Mahmoud *[f]

Received 13th June 2025
Accepted 30th July 2025

DOI: 10.1039/d5ra04212g

rsc.li/rsc-advances

This study developed a lysozyme–dequalinium chloride-loaded Zn–Fe layered double hydroxide (LDH)–chia seed mucilage matrix for enhanced antimicrobial efficacy and sustained drug delivery. The optimized formulation (15% w/v Zn–Fe LDH–chia seed hybrid) achieved encapsulation efficiencies of 93.30 ± 1.92% (lysozyme) and 88.74 ± 1.71% (dequalinium), with a particle size of 153.77 ± 5.79 nm, PDI of 0.18, and zeta potential of +26.44 ± 1.21 mV, ensuring stability and mucoadhesion. Surface morphology, structure, drug loading, and thermostability were confirmed using various techniques. *In vitro* release studies showed sustained drug release over 24 h. Antimicrobial assays demonstrated inhibition zones against *S. mutans* (24.33 ± 2.03 mm), *S. aureus* (14.67 ± 0.88 mm), *S. sobrinus* (11.45 ± 0.887 mm), and *K. pneumoniae* (20.33 ± 2.03 mm). MIC/MBC analysis indicated high susceptibility of *K. pneumoniae* (MIC = 13.00 ± 2.60 μg mL^{-1}, MBC = 20.83 ± 5.23 μg mL^{-1}, $P < 0.001$) and *S. mutans* (MIC = 15.60 ± 1.05 μg mL^{-1}, MBC = 26.07 ± 5.23 μg mL^{-1}, $P < 0.01$), with *S. sobrinus* showing moderate sensitivity (MIC = 49.66 ± 4.32 μg mL^{-1}, MBC = 72.93 ± 6.43 μg mL^{-1}). MBC/MIC ratios below 4 confirmed bactericidal action. The formulation reduced *S. mutans* biofilm formation by 90.1 ± 1.2% at the highest tested concentration. Cytotoxicity evaluation showed a CC50 of 306.6 μg mL^{-1}, demonstrating improved cytocompatibility compared to the free components.

1 Introduction

Dental caries and periodontal diseases remain significant global health challenges, affecting billions of individuals worldwide. These conditions are primarily driven by the colonization and proliferation of pathogenic biofilms, such as *Streptococcus mutans* and *Porphyromonas gingivalis*, on tooth surfaces and within periodontal pockets.[1] Despite the availability of traditional antimicrobial agents, such as chlorhexidine, the emergence of antimicrobial resistance and the potential for adverse effects, such as tooth staining and mucosal irritation, have significantly reduced their effectiveness. Consequently, the limitations of current treatments have driven the need for alternative therapeutic strategies that not only offer potent antimicrobial activity but also minimize side effects and address the underlying challenges of biofilm formation and persistence.[2] Lysozyme, a naturally occurring enzyme found in saliva, tears, and other bodily fluids, plays a critical role in the innate immune system. It exerts its antimicrobial action by hydrolyzing the β-(1,4)-glycosidic bonds in the peptidoglycan layer of bacterial cell walls, leading to cell lysis and death.[3] Beyond its direct antimicrobial effects, lysozyme has been shown to disrupt biofilm formation and enhance the efficacy of other antimicrobial agents.[4] Dequalinium chloride, a bis-quaternary ammonium compound, complements lysozyme by exerting broad-spectrum antimicrobial activity against both Gram-positive and Gram-negative bacteria, as well as fungi. Its mechanism of action involves disrupting bacterial cell membranes and interfering with intracellular processes, making it particularly effective against biofilm-embedded pathogens.[5] Together, lysozyme and dequalinium chloride offer a synergistic, dual mechanism of action, targeting both the structural integrity of bacterial cells and their biofilm-forming

[a]*Material Science and Nanotechnology Department, Faculty of Postgraduate Studies for Advanced Sciences (PSAS), Beni-Suef University, Beni-Suef, 62511, Egypt. E-mail: miramar15@yahoo.com*

[b]*Department of Biology, College of Science, Imam Mohammad Ibn Saud Islamic University (IMSIU), Riyadh 11623, Saudi Arabia. E-mail: asalawam@imamu.edu.sa; harudayni@imamu.edu.sa; aallam@imamu.edu.sa*

[c]*Department of Hygiene, Zoonoses and Epidemiology, Faculty of Veterinary Medicine, Beni-Suef University, 62511, Beni-Suef, Egypt. E-mail: abdelaziz.sahar@yahoo.com*

[d]*Department of Botany and Microbiology, Faculty of Science, Beni-Suef University, Beni-Suef 62511, Egypt. E-mail: abdullah.ali@science.bsu.edu.eg*

[e]*Biotechnology Department, Faculty of Post-Graduate Studies for Advanced Sciences, Beni-Suef University, Beni-Suef, Egypt. E-mail: esraakhaledmahmoud10_pg@psas.bsu.edu.eg*

[f]*Chemistry Department, Faculty of Science, Beni-Suef University, Beni-Suef, 62511, Egypt. E-mail: rami_shafei@science.bsu.edu.eg; rehabkhaled@science.bsu.edu.eg; dr_fatma238@yahoo.com*

capabilities. Existing research has demonstrated the potential of lysozyme and dequalinium chloride for biofilm disruption and antimicrobial therapy, but challenges persist regarding the stability, bioavailability, and sustained release of these agents within the oral cavity. Current drug delivery systems, such as traditional mouthwashes and topical gels, often fail to provide prolonged antimicrobial activity and are susceptible to rapid degradation due to the enzymatic and acidic environment in the mouth. This limitation underscores the necessity for a more advanced, targeted, and sustained-release system capable of overcoming these challenges. Layered double hydroxides (LDHs) have gained attention as versatile nanocarriers for dental applications due to their layered structure, high surface area, and tunable chemical composition, which enable the intercalation and sustained release of therapeutic agents.[6] Zn–Fe LDH has been particularly recognized for its antimicrobial properties, with zinc enhancing the therapeutic potential of LDHs by inhibiting bacterial adhesion and biofilm formation.[7] Iron contributes to the structural stability of LDHs and may also play a role in modulating oxidative stress in periodontal tissues.[8] Despite these advantages, the combination of lysozyme and dequalinium chloride with Zn–Fe LDH matrices for sustained, biofilm-targeting delivery has not been widely explored, and the controlled release of these agents from such a system remains a critical area of innovation. In addition to LDHs, natural biopolymers such as chia seeds have been explored for their potential in drug delivery and dental applications. Chia seeds are rich in mucilage, a polysaccharide-based gel-forming substance that exhibits excellent biocompatibility, mucoadhesive properties, and the ability to sustain the release of encapsulated drugs.[9] When combined with LDHs, chia seed mucilage forms a hybrid matrix that not only enhances the encapsulation efficiency of lysozyme and dequalinium chloride but also provides a protective barrier against enzymatic degradation in the oral cavity.[10] This combination of LDHs and chia seeds represents a novel approach to achieving controlled and targeted delivery of antimicrobial agents in dental applications, addressing the limitations of previous formulations. The integration of lysozyme and dequalinium chloride into a Zn–Fe LDH–chia seed matrix offers several advantages for dental applications. First, the encapsulation of these agents within the matrix protects them from premature degradation in the harsh oral environment, ensuring sustained release at the site of infection.[11] Second, the antimicrobial properties of zinc and iron synergize with those of lysozyme and dequalinium chloride, enhancing the overall efficacy of the formulation against dental pathogens.[12] Finally, the biocompatibility and mucoadhesive properties of chia seeds facilitate the adherence of the formulation to tooth surfaces and periodontal pockets, prolonging its therapeutic effect.[10] In this study, we aim to investigate the development and application of a novel encapsulated formulation combining lysozyme, dequalinium chloride, Zn–Fe LDH, and chia seeds for dental applications. We hypothesize that this formulation will exhibit enhanced antimicrobial activity, sustained drug release, and improved biocompatibility compared to conventional treatments. Through a series of *in vitro* experiments, we seek to demonstrate the potential of this innovative approach to address the limitations of current dental therapies and improve oral health outcomes. Specifically, we aim to provide a more effective solution for biofilm disruption, enhanced antimicrobial efficacy, and prolonged therapeutic effects in the oral cavity.

2 Experimental section

2.1 Materials

Dequalinium chloride (99.52% purity, 456 Da) and lysozyme (from chicken egg whites, 14.3 kDa) were obtained from Sinopharm Chemical Reagent Co., Ltd, Shanghai, China. $Zn(NO_3)_2 \cdot 6H_2O$, $Fe(NO_3)_3 \cdot 9H_2O$, hydroxy ethyl cellulose HEC (product number 434965) of average M_w 90 000 were purchased from Sigma-Aldrich, Missouri, United States. Chia seeds were purchased from Zhengzhou Cheerful Trading Co., Ltd, Henan, China. Sodium benzoate was purchased from Hangzhou Better Chemtech Ltd, Zhejiang, China. Mint (flavouring agent) was purchased from Hangzhou Golden Flavors Co., Ltd, Hangzhou, China. Sodium hydroxide and 37% hydrochloric acid were sourced from Scharlau, Barcelona, Spain. Dimethyl sulfoxide (DMSO) was obtained from Merck, Germany. MTT and trypan blue dye were purchased from Sigma (St. Louis, Mo., USA). Fetal bovine serum, DMEM, HEPES buffer solution, L-glutamine, gentamycin and 0.25% Trypsin–EDTA were purchased from Lonza (Belgium). Sodium dihydrogen phosphate anhydrous, disodium hydrogen phosphate anhydrous, sodium chloride and sodium hydroxide, were obtained from Merck (Darmstadt, Germany). Chlorhexidine was purchased from UNILAB Chemicals & Pharmaceuticals Pvt Ltd, Maharashtra, India.

2.2 Synthesis and formulation development

2.2.1 Synthesis of Zn–Fe LDH. Zn–Fe LDH was synthesized *via* a co-precipitation method. Zinc nitrate and ferric nitrate were dissolved in deionized water at a molar ratio of 2 : 1 (Zn : Fe). The pH of the solution was adjusted to 10 using a 1 M NaOH solution under continuous stirring. The resulting suspension was aged at 60 °C for 24 hours. The precipitate was collected by centrifugation, washed with deionized water until neutral pH, and dried at 60 °C.

2.2.2 Chia seed mucilage powder. Chia seeds were soaked in deionized water (1 : 10 w/v) and stirred at room temperature for 4 hours to allow mucilage powder. Then, the mucilage was separated by filtration and concentrated by freeze-drying (Tofflon FDU-1100 with Capacity up to 1.2 m^2 shelf area, Tofflon Science and Technology Co., Ltd, Shanghai, China) to obtain a dry powder.

2.2.3 Hybrid matrix fabrication. Firstly, Zn–Fe LDH was dispersed in distilled water (1%w/v) with continuous sonication to ensure the uniform dispersion, then freshly prepared chia seed mucilage was gradually added under continuous stirring for one hour in a 1 : 1 ratio to ensure homogeneity.

2.2.4 Encapsulation of bioactives. The encapsulation process was conducted upon three formulations depending on concentration of Zn–Fe LDH–chia seed hybrid, thickening agent (hydroxy ethyl cellulose); Formulation (F1), Formulation (F2),

Table 1 Formulations containing equal amounts of lysozyme and dequalinium chloride, preservative and flavoring agent with variations in Zn–Fe LDH–chia seed hybrid and thickening agent (hydroxy ethyl cellulose) to determine the optimal formulation

Ingredients	Formulation 1 (F1)	Formulation 2 (F2)	Formulation 3 (F3)
Lysozyme (mg)	400	400	400
Dequalinium chloride (mg)	45	45	45
Zn–Fe LDH–chia seed hybrid (%w/v)	5	10	15
Hydroxy ethyl cellulose (mg)	500	750	1000
Flavoring agent (mint)	200	200	200
Sodium benzoate (preservative) (mg)	100	100	100
Purified sterile water (mL)	100	100	100

Formulation (F3), as shown in Table 1. Firstly, Zn–Fe LDH–chia seed hybrid suspension of different concentrations were prepared by dispersing synthesized Zn–Fe LDH–chia seed hybrid powder (5% w/v; F1, 10% w/v; F2, 15% w/v; F3) in sterile water, stirring for 1 hour to achieve uniform dispersion. In a separate step, dissolve lysozyme and dequalinium chloride in sterile water and adjust pH to 6.8 to form a concentration of 0.4% w/v, 0.045%w/v, respectively. Then gradually add the formed solution to each Zn–Fe LDH–chia seed hybrid suspension representing a definite formula under constant stirring for 1 hour, allowing the bioactive compounds to incorporate into the Zn–Fe LDH–chia seed matrix. Filter the mixture to remove unencapsulated compounds, as illustrated in Scheme 1.

2.3 Formulation characterization

2.3.1 Encapsulation efficiency (EE%). The encapsulation efficiency for each formulation was evaluated by measuring the unencapsulated compounds in the supernatant using an Evolution 350 UV-Vis Spectrophotometer (Thermo Fisher Scientific, Massachusetts, USA) from eqn (1) and (2) at wave lengths 282 nm for lysozyme and 327 nm for dequalinium chloride which were selected after a wavelength scan from 200–400 nm exhibiting the maximum absorbance for lysozyme and dequalinium chloride, respectively.

$$\text{Encapsulation efficiency of lysozyme\%} = \frac{\text{total amount of lysozyme} - \text{free lysozyme}}{\text{total amount of lysozyme}} \quad (1)$$

$$\text{Encapsulation efficiency of dequalinium chloride\%} = \frac{\text{total amount of dequalinium chloride} - \text{free dequalinium chloride}}{\text{total amount of dequalinium chloride}} \quad (2)$$

2.3.2 Particle size, PDI, and zeta potential. The Zetasizer Ultra (Malvern, USA) was used to determine the size, dimension, polydispersity index (PDI), and zeta potential of the loaded and unloaded Zn–Fe LDH–chia seed hybrid. The zeta potential and Dynamic Light Scattering (DLS) techniques provide insight into the particle size distribution, surface charge, PDI, and stability of the encapsulated formulation.[13]

2.3.3 Physicochemical properties. Encapsulation efficiency were measured using Thermo-Evolution 350 UV-Vis spectrophotometer (Thermo-Fisher Scientific, Massachusetts, USA). The encapsulated formulation has been characterized using different techniques such as Panalytical (Empyrean) X-ray diffractometer with Cu-Kα radiation (wavelength 0.154 nm) that operated at a current of 35 mA and voltage of 40 kV, scanning at a rate of 8° min^{-1} from 5° to 80° (2θ) was used in X-Ray Diffraction (XRD) investigation, FT-IR using Bruker-Vertex 70 Spectrometer (Germany) apparatus covering the wave number range of 4000–400 cm^{-1} was used for Fourier Transform Infrared Spectroscopy (FTIR) investigation. Also, the Zetasizer Ultra (Malvern, USA) was used to determine the size, dimension, polydispersity index (PDI), and zeta potential of the loaded and unloaded LDH–chia seed hybrid.[13]

The crystallite sizes (D) of prepared materials were calculated using Deby–Sherrer's, which is expressed by the following formula:

$$D = \frac{0.9\lambda}{\beta \cos(\theta)} \quad (3)$$

where β is full width at half maximum (FWHM) at the diffraction angle 2θ, λ = X-ray wavelength. The interatomic spacing was investigated from Bragg's law as.[14,15]

$$2d \sin(\theta) = n\lambda \quad (4)$$

n is the order of the reflection (usually 1 for XRD), λ is the wave length of X-ray (commonly 1.5406 A for Cu Kα radiation), d is the interplanar spacing of the crystal lattice plane, θ is the diffraction angle (half of the 2θ angle in XRD).

The degree of crystallinity X_c for all prepared samples was estimated from eqn (5) to determine the impact of chia addition on the crystalline structure alterations of the host matrix.[16]

$$X_c = \frac{\text{area of the crystalline peaks } (A_c)}{\text{area of all peaks (crystalline } (A_c) + \text{amorphous } (A_a))} \quad (5)$$

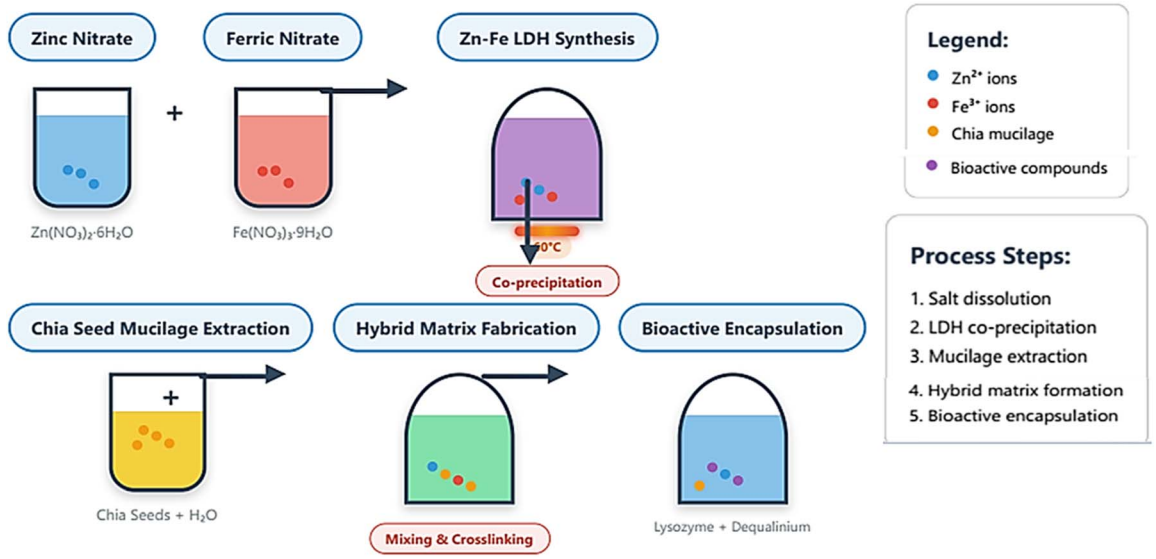

Scheme 1 Illustration of the stepwise fabrication of the Zn–Fe LDH–chia seed hybrid Matrix, including the synthesis of Zn–Fe LDH, powder of chia seed mucilage, hybrid matrix formation, and encapsulation of lysozyme and dequalinium chloride.

A_c and A_a were determined from the convolution of the XRD peaks using Fityk software.[17]

The microstructure was examined *via* an EVO MA10 scanning electron microscope (ZEISS, Germany). Elemental mapping analyses were conducted *via* a Quanta FEG250-FEI SEM instrument (USA). Additionally, BET analysis was conducted to assess the specific surface area, pore size distribution, and specific pore volume of the modified prepared materials *via* TriStar II 3020 from Micrometrics. Thermal gravimetric analysis (TGA) was performed at a rate of 10 °C min^{-1} in a N_2 atmosphere (Netzsch; STA 409 PC/PG). Finally, quantitative determinations of the residual drugs concentration using an Evolution 350 UV-Vis Spectrophotometer (Thermo Fisher Scientific, Massachusetts, USA).

2.4 *In vitro* release and kinetics

In this study, we used Phosphate-Buffered Saline (PBS of pH 6.8) to simulate saliva, firstly, we mixed 38.5 mL of 0.2 M NaH_2PO_4, 61.5 mL of 0.2 M Na_2HPO_4, and 100 mL of 1.5 M NaCl, then dilute to 1 L with distilled water. Adjust the pH to 6.8 using NaH_2PO_4 (to lower pH) or Na_2HPO_4 (to raise pH). Firstly, the dialysis bags were soaked in the dissolution (release) medium overnight. Then, 100 mg of encapsulated Formulation (F3) and 100 mg of unencapsulated formulation (control test) were placed in dialysis bags made of cellulose membrane (molecular weight cut-off of 14 000 Da, SERAVA Electrophoresis) that were sealed at both ends with thermo-resistant thread. These bags were immersed in a glass jar containing 100 mL of phosphate buffer solution (PBS, pH 6.8, at 37 °C ± 0.5 °C) to mimic physiological conditions. The jar was then placed in a shaker incubator (Labsol, India), and it was set at 100 rpm to simulate mild agitation in the oral cavity. At predefined time intervals (15 min, 30 min, 1 h, 2 h, 4 h, 6 h, 8 h, 12 h and 24 h), 2 mL of the PBS surrounding the dialysis bag was withdrawn and replaced with an equal volume of fresh PBS to maintain sink conditions. Each sample was filtered through a 0.22 μm nylon syringe filter. The concentration of both of lysozyme and dequalinium released into the surrounding medium was measured using an Evolution 350 UV-Vis Spectrophotometer (Thermo Fisher Scientific, Massachusetts, USA) at wave lengths 282 nm for lysozyme and 327 nm for dequalinium chloride. The cumulative drug release percentage was calculated by plotting the concentration of released lysozyme and dequalinium against time, allowing for an evaluation of the release profile of the encapsulated lysozyme and dequalinium from Zn–Fe LDH–chia seed hybrid compared to the free drugs. Drug release at time t, cumulative drug release (%) were calculated using eqn (6) and (7):

$$\text{Released drug at time } t = C_t \times V \quad (6)$$

where, C_t represents the drug concentration at time t (mg mL^{-1}), V represents volume of the dissolution medium (mL).

$$\text{Cumulative drug release (\%)} = \frac{\text{released drug at time } t}{\text{initial amount of drug loaded}} \times 100 \quad (7)$$

Various release kinetics models were applied including zero-order kinetics (constant release rate), first-order kinetics (release rate depends on the amount of drug remaining), Korsmeyer–Peppas model (power law), Higuchi model (diffusion-controlled release) to give insight into the release mechanism either through diffusion, swelling, or erosion of the encapsulated formulation using the following equations:

Zero-order kinetics

$$M_t = M_0 + Kt \quad (8)$$

First-order kinetics

$$\frac{M_t}{M_0} = 1 - e^{-k_1 t} \quad (9)$$

Korsmeyer–Peppas Model

$$\frac{M_t}{M_0} = Kt^n \quad (10)$$

Higuchi model

$$M_t = K_H\sqrt{t} \quad (11)$$

M_t = amount of drug released at time t, M_0 = initial amount of drug, k_1 = first-order rate constant, n is the release exponent that indicates the release mechanism, t = time, k_H = Higuchi rate constant (depends on properties like the diffusion coefficient, solubility, and surface area).

2.5 Biological evaluations

2.5.1 Antimicrobial activity. Clinical isolates of *Escherichia coli* (*E. coli*), *Klebsiella pneumoniae* (*K. pneumoniae*), *Pseudomonas aeruginosa* (*P. aeruginosa*), *Staphylococcus aureus* (*S. aureus*), and *Streptococcus mutans* (*S. mutans*) were recovered from dairy cattle exhibiting clinical mastitis. These isolates were used to evaluate the antimicrobial efficacy of chia seeds and synthesized nanoparticles. The bacterial isolates were stored as stock cultures at −20 °C in the Laboratory of Hygiene, Zoonoses, and Epidemiology at the Faculty of Veterinary Medicine, Beni-Suef University. The isolates were initially recovered and identified using standard biochemical protocols.[18] Prior to the experiments, all bacterial isolates, including *S. mutans*, were cultured overnight in nutrient broth (Oxoid Ltd, UK) at 37 °C under aerobic conditions. To achieve a concentration of 1×10^5 colony-forming units per mL (CFU mL^{-1}), equivalent to 0.5 McFarland standard, a small number of colonies were suspended in 0.9% saline (NaCl). For the chemical suspensions, chia seeds, Zn–Fe layered double hydroxides (LDHs), and the encapsulating formula were prepared at a concentration of 1000 μg mL^{-1}. These materials were suspended in 10.0% dimethyl sulfoxide (DMSO, Sigma-Aldrich, USA) and sonicated for 3–5 minutes using a high-power sonicator (20 kHz, Model: Q700 Sonicator®, Australia).

2.5.2 Agar well diffusion. The antimicrobial activity of the prepared compounds was assessed using the standard agar well diffusion method. Each bacterial inoculum, including *S. mutans*, was streaked separately onto the surface of Mueller–Hinton agar (MHA, Sigma-Aldrich, Dorset, UK). After the agar solidified, four circular wells (6 mm in diameter) were created in each plate using a sterile cork borer. Each well was filled with 35–50 μL of the prepared chemical suspensions. The plates were incubated at 37 °C for 24 hours, after which the inhibition zones were measured. Ciprofloxacin (5 μg, Oxoid) was used as a positive control, and 10.0% DMSO served as the negative control. All experiments were performed in triplicate, and the results were expressed as means ± standard error (SE).

2.5.3 Minimum inhibitory concentration (MIC) and minimum bactericidal concentration (MBC). The MIC and MBC of the tested nanoparticles against the selected bacterial isolates were determined using the broth macro-dilution method.[18] Briefly, each nanoparticle suspension was serially diluted in 1 mL of sterile Mueller–Hinton broth (Oxoid Ltd, UK), starting from an initial concentration of 1000 μg mL^{-1}. Bacterial inoculum (1×10^5 CFU mL^{-1}) was added to each dilution, and the tubes were incubated at 37 °C for 24 hours. After incubation, 100 μL of the lowest concentration showing no visible turbidity was streaked onto Mueller–Hinton agar (MHA) and incubated overnight at 37 °C under aerobic conditions. The MIC was defined as the lowest concentration of the tested material that inhibited visible bacterial growth in the broth. The MBC was determined as the lowest concentration that resulted in 100% bacterial killing, with no growth observed on the agar surface. All experiments were conducted in triplicate. Additionally, the MBC/MIC ratio was calculated to determine whether the tested compounds exhibited bacteriostatic or bactericidal activity.

2.5.4 Anti-biofilm assay. As described by Christensen *et al.*,[19] a qualitative assay was performed to assess the suppression of biofilm development in the presence and absence of synthesized Zn–Fe LDH–chia seed hybrid formulations (F1, F2, F3). The inner surfaces of the tubes were visually examined for biofilm formation with and without the application of these formulations. The anti-biofilm effectiveness of the synthesized materials was tested against *S. mutans* and compared to an untreated control.[20]

2.5.5 Preparation and inoculation. 5 mL of nutrient broth (NB) was added to the tubes, which were then inoculated with cultures adjusted to 0.5 McFarland standards, resulting in concentrations of 1–2.5 × 10^8 CFU mL^{-1}.

2.5.6 Incubation and rinsing. The tubes were incubated for 24 hours at 37.0 ± 0.5 °C. After incubation, the contents were discarded, and the tubes were rinsed with phosphate-buffered saline (PBS, pH = 7.0) and allowed to dry.

2.5.7 Fixation and staining. Bacterial cells adhered to the tube walls were fixed using 5 mL of 3.0% sodium acetate for 15 minutes, followed by rinsing with deionized water. The biofilms were stained with 0.1% crystal violet (CV) dye for 15 minutes, and excess dye was removed by washing.

2.5.8 Semi-quantitative assessment. For semi-quantitative analysis, 5 mL of absolute ethanol was added to dissolve the CV-stained biofilms. The optical density (OD) of the dissolved biofilms was measured using ultraviolet-visible (UV-Vis) spectrophotometry at a wavelength of 570 nm.[21] The percentage of biofilm inhibition was calculated using the following equation:

$$\text{Biofilm inhibition } \% = \frac{[\text{OD of untreated sample} - \text{OD of treated sample}]}{\text{OD of untreated sample}} \times 100 \quad (12)$$

2.5.9 Cytotoxicity assay

2.5.9.1 Cell lines and culture conditions. Human gingival fibroblast cells (HGF-1 cell line; ATCC® CRL-2014) were

obtained from the American Type Culture Collection (ATCC; Manassas, VA, USA). These cell lines were propagated and tested for cytotoxicity assays at the Tissue Culture Unit of the Regional Center for Mycology and Biotechnology, Al-Azhar University. The cells were cultured in Dulbecco's Modified Eagle's Medium (DMEM) supplemented with 10% heat-inactivated fetal bovine serum, 1% L-glutamine, HEPES buffer, and 50 μg per mL gentamycin. All cells were maintained at 37 °C in a humidified atmosphere containing 5% CO_2 and were subcultured twice a week. The study included four groups: Group 1 consisted of human gingival fibroblasts treated with Sample 1 (Formulation 1), Group 2 included human gingival fibroblasts treated with Sample 2 (Formulation 2), Group 3 involved human gingival fibroblasts treated with Sample 3 (Formulation 3), and Group 4 served as the control group, consisting of untreated human gingival fibroblasts cultured in DMEM medium.

2.5.9.2 Cytotoxicity evaluation via MTT assay. For cytotoxicity assessment, the cells were seeded into a 96-well plate at a density of 1×10^4 cells per well in 100 μl of growth medium. After 24 hours of seeding, 100 μl of the tested samples were added to the confluent cell monolayers in the 96-well plates. Each concentration of the test sample was tested in triplicate. Control cells were incubated without the test sample. The plates were incubated at 37 °C in a humidified incubator with 5% CO_2 for 24 hours. After 24 hours of incubation, cell viability was assessed using the MTT assay. The media was removed from the wells and replaced with 100 μl of fresh culture DMEM medium without phenol red. Then, 10 μl of a 12 mM MTT stock solution (5 mg of MTT in 1 mL of PBS) was added to each well, including untreated controls. The plates were incubated at 37 °C and 5% CO_2 for 4 hours. Following incubation, 85 μl of the media was removed from each well, and 50 μl of DMSO was added to dissolve the formazan crystals. The plates were incubated for an additional 10 minutes at 37 °C.

The optical density (OD) was then measured at 590 nm using a microplate reader (TS800, BioTek, Inc, USA) to determine the number of viable cells. Cell viability was calculated as:

$$\text{Viability}(\%) = \frac{[\text{OD}_t]}{[\text{OD}_c]} \times 100 \quad (13)$$

where OD_t is the mean optical density of wells treated with the tested sample and OD_c is the mean optical density of untreated cells.

The relationship between cell survival and drug concentration was plotted to obtain the survival curve for each treatment. The cytotoxic concentration (CC50), defined as the concentration required to induce toxic effects in 50% of the cells, was determined from the dose–response curve using GraphPad Prism software (San Diego, CA, USA).

2.6 Statistical analysis

The experimental results were analyzed using one-way analysis of variance (ANOVA) at a significance level of $p < 0.05$. All statistical analyses were performed using the Statistical Package for the Social Sciences (SPSS) software. Standard errors of treatment means were also calculated. Additionally, OriginPro software (version 9.0) was used for data visualization and further statistical evaluation.

2.7 Computational details

To elucidate the adsorption interactions and mechanism of action in the studied system, simple density functional theory (DFT) calculations were performed using ORCA 6.0 suite of programs.[22–26] The adsorption of glucuronic acid (representing chia seed mucilage), dequalinium cation, and aspartic acid (Asp52, modeling lysozyme's active site) on a Zn–Fe LD surface, specifically $[Fe_2Zn_5(OH)_{24}]^{8-}$ cluster, was investigated using density functional theory (DFT) with ORCA 6.0, employing the

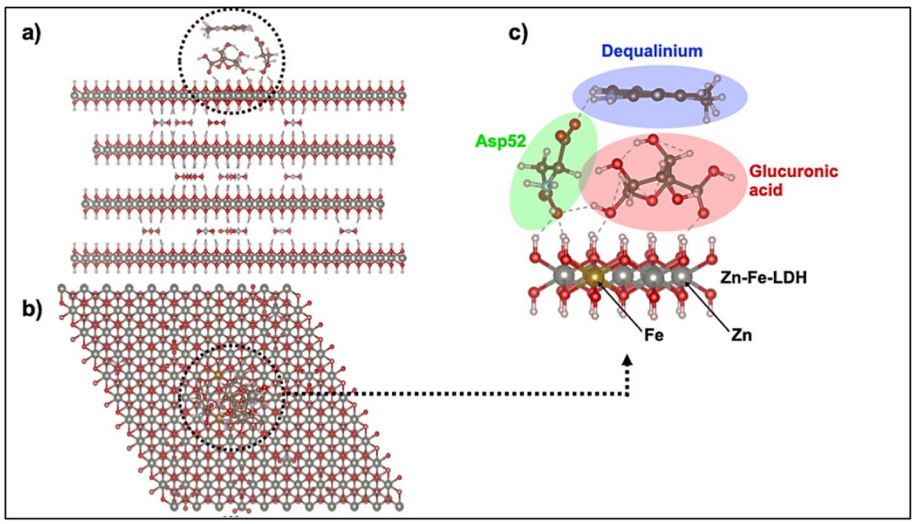

Fig. 1 (a) Side and (b) top views of DFT-optimized structure of the whole system. (c) The QC includes the glucuronic acid (in red circle), dequalinium cation (in blue circle), Asp52 (in green circle), and Zn–Fe-LDH (gray and golden spheres for Zn^{2+} and Fe^{2+} ions, respectively), showing hydrogen bonds (gray dashed lines).

QMMM embedded cluster approach.[27,28] The system used is show in Fig. 1(a and b), and the quantum cluster is given in Fig. 1(c) while the rest of the Zn–Fe LDH part is treated as point charges. The B3LYP functional with D3BJ dispersion correction and def2-SVP basis set of the Ahlrichs group was employed, incorporating the conductor-like polarizable continuum model (C-PCM) with water solvation model to mimic the aqueous oral environment.[29–35] Geometries were optimized at this level of theory, followed by single-point energy calculations for the full system (glucuronic acid + Asp52 + dequalinium + Zn–Fe-LDH), individual components, and pairwise systems (glucuronic acid + Zn–Fe-LDH, Asp52 + Zn–Fe-LDH, and dequalinium + Zn–Fe-LDH). Basis set superposition error (BSSE) was corrected using the counterpoise method, treating each component as a fragment. Interaction energies were computed *via* the supermolecular approach: ($\Delta E_{\text{int}} = E_{\text{complex}} - \sum E_{\text{fragment}}$), with results summarized in Table 2.

CHELPG charges were calculated to analyze electrostatic interactions, with interatomic distances extracted from the optimized geometry to identify hydrogen bonds and electrostatic interactions.

pH-responsive behavior of LDH was adjusted by the incorporation of a surface SiOH group, following the methodology proposed in previous studies. Two drug molecules were studied: lysozyme was approximated by a simplified model molecule $C_6H_4OHNH_2$ (phenolic amine), representing its key functional groups responsible for adsorption. Dequalinium was used as the second drug molecule without further simplifications. Both drug molecules and LDH models were investigated in their neutral and anionic states to simulate protonation/deprotonation events occurring under different pH conditions. All geometries (isolated drugs, isolated LDH, and drug–LDH complexes) were optimized without symmetry constraints. Frequency calculations were performed to ensure that the structures correspond to true minima (no imaginary frequencies). In this study, the pH dependence of the binding energies of the drugs with the LDH carrier is modeled by considering the protonation and deprotonation processes of both the drug molecules and the carrier complex. The protonation and deprotonation states of the complexes are assumed to shift according to the pK_a values of the drug and the carrier. For each pH, the protonation state of the drug is determined by the Henderson–Hasselbalch equation, which relates the protonation equilibrium of a molecule to the pH and its pK_a value. The protonated form dominates at lower pH, and the deprotonated form becomes more prevalent at higher pH. For each pH value, the protonation state of the drug and the carrier is updated, and the corresponding interaction energies are calculated using DFT. The total energy of the system is then obtained by considering the individual energies of the protonated and deprotonated species and their interactions. The final adsorption energies are computed by taking into account the changes in the protonation states of the drug and the LDH carrier at each pH value. This methodology allows for the prediction of the pH-dependent loading and release behaviors of the drugs in response to the changes in the protonation states, which is crucial for understanding their absorption and release mechanisms at different pH conditions as described in this study.[36] The interaction energy (E_{int}) was calculated using the formula:

$$E_{\text{int}} = E_{\text{complex}} - (E_{\text{LDH}} + E_{\text{drug}})$$

where, E_{complex} is the total energy of the optimized drug–LDH system, E_{LDH} is the total energy of the isolated LDH, and E_{drug} is the total energy of the isolated drug. The pH-responsive loading and release mechanism was evaluated by examining the variation of the interaction energy (E_{int}) under different protonation states of the drug and LDH.

Table 2 DFT-calculated interaction energies (in kcal mol^{-1}) for the adsorption of individual ligands (dequalinium, glucuronic acid, Asp52) and the combined ligand system on Zn–Fe–LDH

System	Interaction energy (kcal mol^{-1})
Dequalinium + Zn–Fe-LDH	−371
Glucuronic acid + Zn–Fe-LDH	−115
Asp52 + Zn–Fe-LDH	−92
Glucuronic acid + Asp52 + dequalinium + Zn–Fe-LDH	−343

3 Results and discussion

3.1 Formulation optimization and characterization

Encapsulation efficiency (EE%) is a critical parameter for assessing the effectiveness of a drug delivery system, as it directly reflects the ability of the carrier matrix to incorporate and retain active agents. A higher EE% indicates that a larger proportion of the therapeutic agents remain encapsulated within the matrix, thereby reducing the likelihood of degradation or premature release. This ensures a more controlled, sustained release profile at the target site, maximizing the therapeutic potential. In our study, Formulation 3 exhibited the highest EE% for both lysozyme and dequalinium chloride, suggesting that the higher concentration of the Zn–Fe LDH–chia seed hybrid (15% w/v) enhances the matrix's stability and its capacity to encapsulate the active agents more effectively. This finding is in line with previous studies showing that increasing the concentration of the carrier matrix improves the entrapment of bioactive compounds due to the availability of more binding sites and a denser network structure.[37–39] However, the novelty of our approach lies in the incorporation of chia seed mucilage, which plays a pivotal role in modulating the release kinetics of the encapsulated agents. The chia seed mucilage forms a gel-like barrier that limits the diffusion of bioactive agents, providing a controlled, delayed release. This is attributed to its polysaccharide-rich composition, which interacts with the Zn–Fe LDH matrix and the encapsulated therapeutics, resulting in a stable hybrid complex. The unique combination of Zn–Fe LDH with chia seed mucilage offers not only enhanced encapsulation but also a prolonged therapeutic effect, making it highly suitable for oral applications, such as mouthwash formulations.

The particle size, PDI, and zeta potential of the encapsulated formulation are critical for its stability, mucoadhesion, and bioavailability in the oral cavity. F3 exhibited the smallest particle size, lowest PDI, and highest zeta potential, indicating superior stability and uniformity. The smaller particle size enhances the penetration of the formulation into biofilms and periodontal pockets, while the higher zeta potential ensures better colloidal stability and mucoadhesion. The low PDI value (0.18) further confirms the homogeneity of the formulation, which is essential for consistent drug release.[40–42] Table 3 shows the Particle size distribution, polydispersity index (PDI) and zeta potential for loaded and un loaded Zn–Fe LDH–chia seed hybrid. Table 3 shows the encapsulation efficiency of lysozyme and dequalinium in Zn–Fe LDH–chia seed hybrid in addition to particle size, zeta potential and PDI.

3.2 Structural and morphological analysis

The strong and sharp diffraction peaks of Zn–Fe LDH at low 2θ values in the range of 2θ = 6–80°. The LDH phase's basal spacing value, which is the brucite-like layer's thickness added together (0.414 nm) (Fig. 2 a), is in good agreement with the nitrate LDH materials' reference code (04-018-3495). The presence of the main peaks at 2θ at 9.14°, 25.34°, 31.86°, 39.01°, 47.70°, and 56.90° confirms the layered structure of the Zn–Fe LDH. The absence of free hydroxide formation in the XRD chart could be attributed to the delayed addition of sodium hydroxide during the formation of LDH. We note that the peaks are narrow, indicating that Zn and Fe were substituted into the crystalline Zn–Fe LDH structure.[43] The plane indices were included to the XRD profile and compared with JCPDS reference file. The XRD analysis of the LDH–chia hybrid and Lys–Dqm/LDH–chia hybrid composites (Fig. 2b), as illustrated in Fig. 2a, reveals the presence of various mineralogical phases within the created materials. The synthesized Zn–Fe LDH–Chia material displayed distinct diffraction peaks at (003), (006), (009), (012), (015), (018), (110), (113), (112)and (201) of Zn–Fe LDH [JCPDS No. 38-0486],[44] which were attributed to the crystallographic structure of the material (JCPDS Card No. 38-0486). The XRD pattern shows a peak for chia seed powder at approximately 2θ = 12.37° in the two prepared samples, but another weak peak was observed only at approximately at 2θ = 19.50° in the Zn–Fe

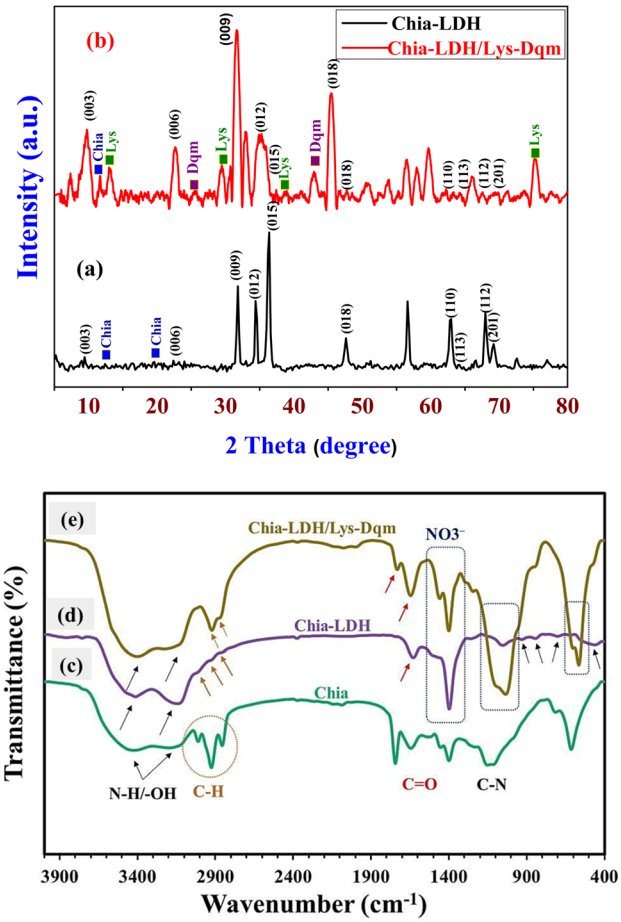

Fig. 2 (a) XRD of LDH–chia hybrid, (b)LDH–chia–Lys–Dqm hybrid composite, (c) FTIR spectrum analysis of chia seed powder, (d) LDH–chia hybrid, and (e) Lys–Dqm/LDH–chia hybrid materials.

LDH–chia sample. Following the incorporation of Lys and Dqm into the LDH–chia hybrid to form the Lys–Dqm/LDH–chia composite, X-ray diffraction analysis revealed a significant reduction in peak intensities, complete disappearance of certain reflections, and pronounced broadening of some remaining diffraction peaks. This phenomenon may be attributed to the intercalation of Lys and Dqm within the interlayer spaces of LDH was related to the decrease if the crystallite size

Table 3 Characterization of encapsulated formulations: particle size, zeta potential, and encapsulation efficiency of lysozyme and dequalinium[a]

Formulation	%w/v of Zn–Fe LDH–chia seed hybrid	Mean particle size (diameter in nm)	Dispersity (PDI)[b]	Zeta potential (mV)	Encapsulation efficiency (EE%)	
					Lysozyme	Dequalinium
Blank (Zn–Fe LDH–chia seed hybrid)	—	106.44 ± 3.46	Monomodal	+30.24 ± 1.57	—	—
Formulation 1	5%	222.46 ± 4.15	Monomodal	+18.12 ± 2.13	75.01 ± 1.23	70.11 ± 2.03
Formulation 2	10%	184.42 ± 4.78	Monomodal	+21.08 ± 1.98	82.33 ± 2.26	78.20 ± 1.15
Formulation 3	15%	153.77 ± 5.79	Monomodal	+26.44 ± 1.21	93.30 ± 1.92	88.74 ± 1.71

[a] Data are expressed as means ± SE (mean ± SE, n = 3). [b] Polymodal refers to PDI values that exceed 0.3, while monomodal refers to PDI values below 0.3.

of the material after loading to 10.58 nm, ultimately leading to a reduction in its crystallinity.[45] Also, a small peak shift can be seen for the (003) peak which can be attributed to intercalation of the drugs loaded into the LDH layers. Additionally, new diffraction peaks observed at 13.18, 29.82°, 35.42°, and 75.38°,[46] indicate the presence of the Lys crystalline phase (ICDD PDF Number: 00-045-0192), while additional peaks corresponding to Dqm were identified at 22.78°, 28.42°, and 43.5°,[47] further supporting the structural modifications. Consequently, the identification of XRD patterns associated with all incorporated components validates the successful creation of the Lys–Dqm/LDH–chia hybrid composite. The basal plane of (003) has been decreased from 9.78 Å for LDH[48] to 9.40 Å for chia–LDH and 8.88 Å for chia–LDH/Lys–Dqm, respectively. This may be indicate that the chia was covered the surface and the loaded drugs interacted on the surface because the *d* spacing decrease after loading.[45]

Fig. 2c–e provides a comprehensive representation of the FTIR spectra for the materials chia seed powder, chia–LDH hybrid, and chia–LDH/Lys–Dqm hybrid materials, highlighting distinctions in their molecular vibrational modes and functional group characteristics. The absorption bands identified at 3442.74 cm^{-1} and 1645.19 cm^{-1} correspond to the stretching and bending vibrations of hydroxyl groups associated with physically adsorbed water.[49,50] The FTIR spectrum of the chia seed powder demonstrated significant absorption peaks within the range of 1745–1460 cm^{-1}, corresponding to the stretching vibrations of the C=O bond, thereby confirming the presence of a ketone functional group.[51,52] Additionally, the spectrum revealed a peak at 1159.15 cm^{-1}, characteristic of the C–N stretching vibration, and another peak near 3006.58 cm^{-1}, indicative of the stretching vibration of alkane (C–H) groups.[51] The absorption bands observed within the range of 2923–2850 cm^{-1} correspond to the stretching vibrations of C–H bonds, specifically associated with the methyl and methylene groups forming the structural backbone of lipids.[52] Furthermore, the band observed at 714 cm^{-1} is associated with the bending vibrations of methylene groups found in *cis*-disubstituted olefins.[53] The synthesis of the LDH–chia hybrid leads to the elimination and displacement of certain absorption bands associated with the chia seed powder, accompanied by the appearance of a novel absorption peak noticed at 1396.38 cm^{-1}. This newly observed band is attributed to the stretching vibrations of NO_3^- groups, which are integrated within the structural framework of the fabricated chia–LDH hybrid.[54] All vibrational bands identified below 850 cm^{-1} are attributed to the characteristic oscillations of the metal–oxygen lattice, encompassing M–O, M–OH, and M–O–M bonding interactions.[55] The combination of Lys and Dqm into the chia–LDH confirmed by the presence of distinct transmittance bands at 1072.63 cm^{-1} and 1396.38 cm^{-1}, assigned to Lys.[56,57] Additionally, the presence of strongly enhanced bands within the range of 1000–1300 cm^{-1} (corresponding to C–N stretching vibrations) and 2800–3000 cm^{-1} (associated with C–H stretching vibrations) provided clear evidence of Dqm integration within the fabricated composite structure. The spectroscopic modifications observed in characteristic FTIR vibrational modes, accompanied by significant shifts in baseline transmittance profiles following Lys–Dqm intercalation, demonstrate direct correlation with the XRD structural evolution. This manifests through: attenuation of characteristic LDH diffraction peaks, and emergence of distinct crystalline shoulders corresponding to Lys and Dqm molecular packing. These complementary analytical observations collectively validate the successful integration of bioactive compounds within the chia–LDH matrix. This multimodal spectroscopic evidence substantiates the formation of the chia–LDH/Lys–Dqm nanocomposite, enabling the proposition of a coherent mechanistic framework for its successful fabrication.

Fig. 3 illustrates the structural morphology of both the LDH–chia and Lys–Dqm/LDH–chia hybrid nanocomposites, as analyzed through FESEM images captured at varying magnifications. As demonstrated in Fig. 3a and b, the FESEM analysis of the LDH–chia hybrid nanocomposite reveals a distinctive flaky morphology, characterized by a plate-like structure with varying particle sizes. This structure is characterized by a rough, porous exterior and a two-dimensional nanosheet morphology, which significantly enhances the available surface area and provides abundant active sites to facilitate biomedical activities. Fig. 3a and b reveal elongated, rough surface features, with entangled chia particles embedded within and coating the Zn–Fe LDH sheets, a configuration that likely enhances surface roughness and subsequently improves the material's reactivity. The combination of Lys and Dqm substances to the LDH–chia hybrid (Fig. 3d and e) facilitates the formation of semi-euhedral nanoparticles that are uniformly distributed and bonded together, afterward evolving into layered structures that establish a three-dimensional networked framework. Moreover, the observed morphological transition from a flaky to a networked structure in Fig. 3d and e can be attributed to the intercalation of Lys and Dqm molecules within the Zn–Fe LDH interlayers (Fig. 3a and b), which induces that characteristic morphology and their subsequent reorganization into a three-dimensional porous network through drug–matrix interactions, thereby confirming the successful formation of a stable hybrid nanocomposite with enhanced structural integration. These modifications in texture result in a substantial elevation of surface roughness, which generates a more varied topographical configuration and an augmentation of the composite's overall porosity. This improvement is expected to favorably impact both the total surface area and the biochemical interactions of the composite, consequently enhancing its effectiveness for medical applications. Also, Fig. 3 illustrates the structural morphology of both the LDH–chia hybrid and Lys–Deq/LDH–chia hybrid composites, as analyzed through FESEM images captured at varying magnifications and 2D/3D projection of topographical configuration for surface roughness. A rough, porous exterior and holes with a two-dimensional nanosheet morphology (image c) characterize the good structure. This good structure significantly enhances the available surface area and provides abundant active sites to facilitate biomedical activities. The combination of Lys and Deq substances to the LDH–chia hybrid (Fig. 3(d and e)) facilitates the formation of semi-euhedral nanoparticles that are uniformly distributed and

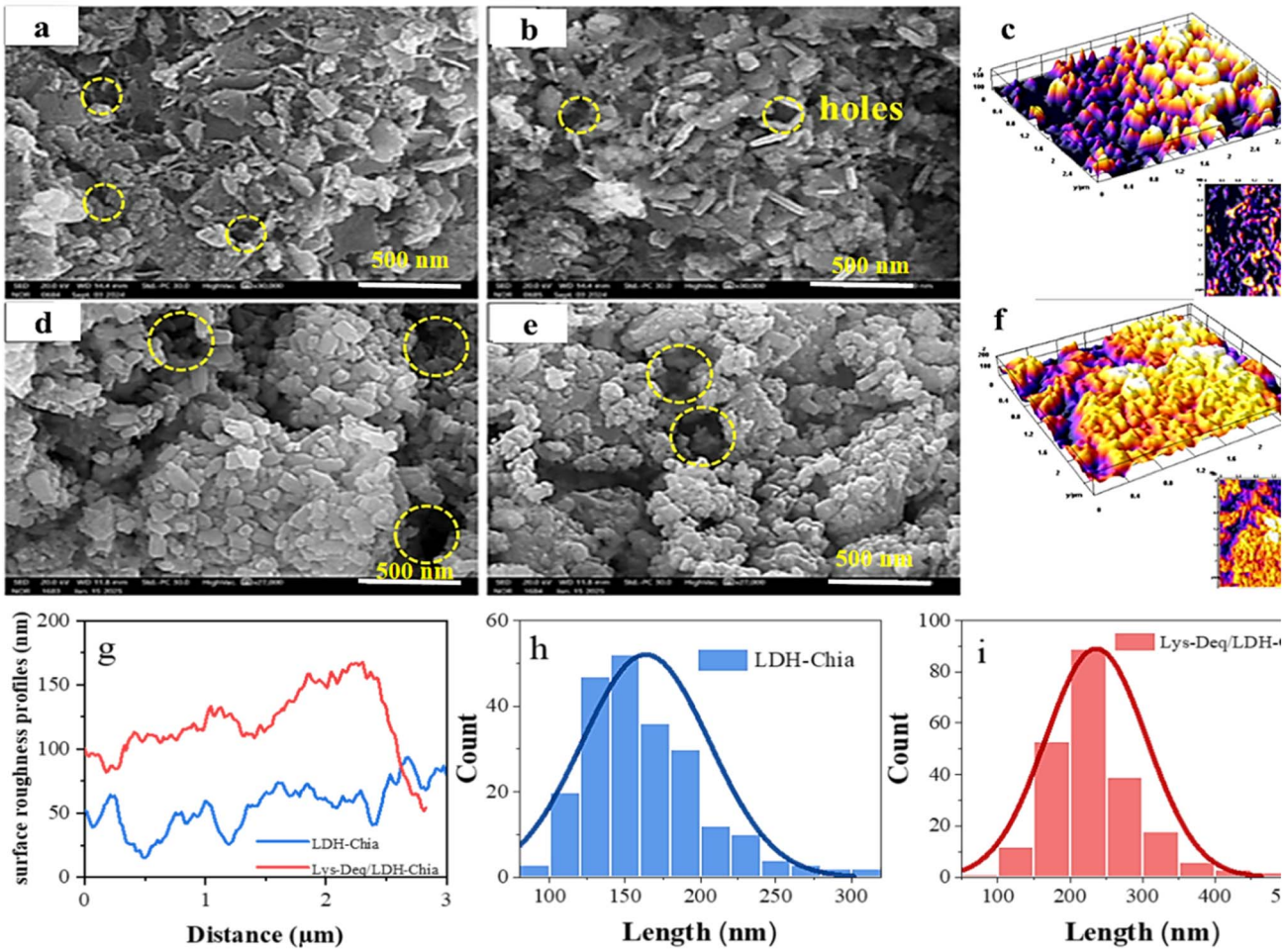

Fig. 3 FESEM micrographs of LDH–chia hybrid (a and b) and Lys–Deq/LDH–chia hybrid composite (d and e). Topographical configuration of LDH–chia hybrid (c) and Lys–Deq/LDH–chia hybrid composite (f). Topographical cross section (g), length distributions of LDH–chia hybrid (h) and of Lys–Deq/LDH–chia hybrid composite (i).

bonded together, afterward evolving into layered structures that establish a 3D networked framework. A topographical study of Lys–Deq/LDH–chia hybrid composite is shown in Fig. 3f, while a cross section of both LDH–chia hybrid material and Lys–Deq/LDH–chia hybrid composite is observed to illustrate the differences. These modifications in texture result in a substantial elevation of surface roughness, which generates a more varied topographical configuration and an augmentation of the composite's overall porosity and holes. The length distributions of LDH–chia hybrid material and Lys–Deq/LDH–chia hybrid composite was traced in Fig. 3(h and i) and it was found that the average lengths reached 164 nm and 237 nm, respectively. This improvement is expected to favorably impact both the total surface area and the biochemical interactions of the composite, consequently enhancing its effectiveness for medical applications.

In order to gain insight into the distribution of the elements inside the composite LDH, an elemental study was performed using Map-EDX. The components of LDH–chia–Lys–Dqm hybrid composite were results confirmed that carbon made up 3.4%, oxygen made up 25.5%, nitrogen made up 0.5%, zinc made up 65.9%, and iron made up 4.6% (Fig. 4) that confirms the presence of the Lys–Deq in the composite LDH hybrid (Table S1).

Fig. 5 shows the nitrogen adsorption–desorption behaviour of the synthesized Lys–Deq/LDH–chia composite. The presence of both Type I Type IV isotherms with noticeable hysteresis loops suggests mesoporous characteristics, likely caused by particle aggregation (Fig. 5a and b).[58] The surface area of the powder LDH–chia hybrid composite was observed at 41.065 m^2 g^{-1}, while after applying the loading by Lys–Deq experiments, the surface area was followed to reach 35.892 m^2 g^{-1} in Fig. 5(c and d). Consequently, the Barrett–Joyner–Halenda model (BJH) method showed that the average pore area was 12.67 nm for the powder LDH–chia hybrid composite, while it was 15.23 nm after loading of Lys–Deq experiments. As nitrogen is adsorbed and the relative pressure rises, the material becomes denser. The desorption curve reveals a hysteresis loop which is a typical indicator of mesoporous structures with pore sizes ranging from 2 to 50 nm. Thus, porosity plays a crucial role in the performance of Lys–Deq/LDH–chia hybrid composite. However, when particles aggregate after loading during experiments, they

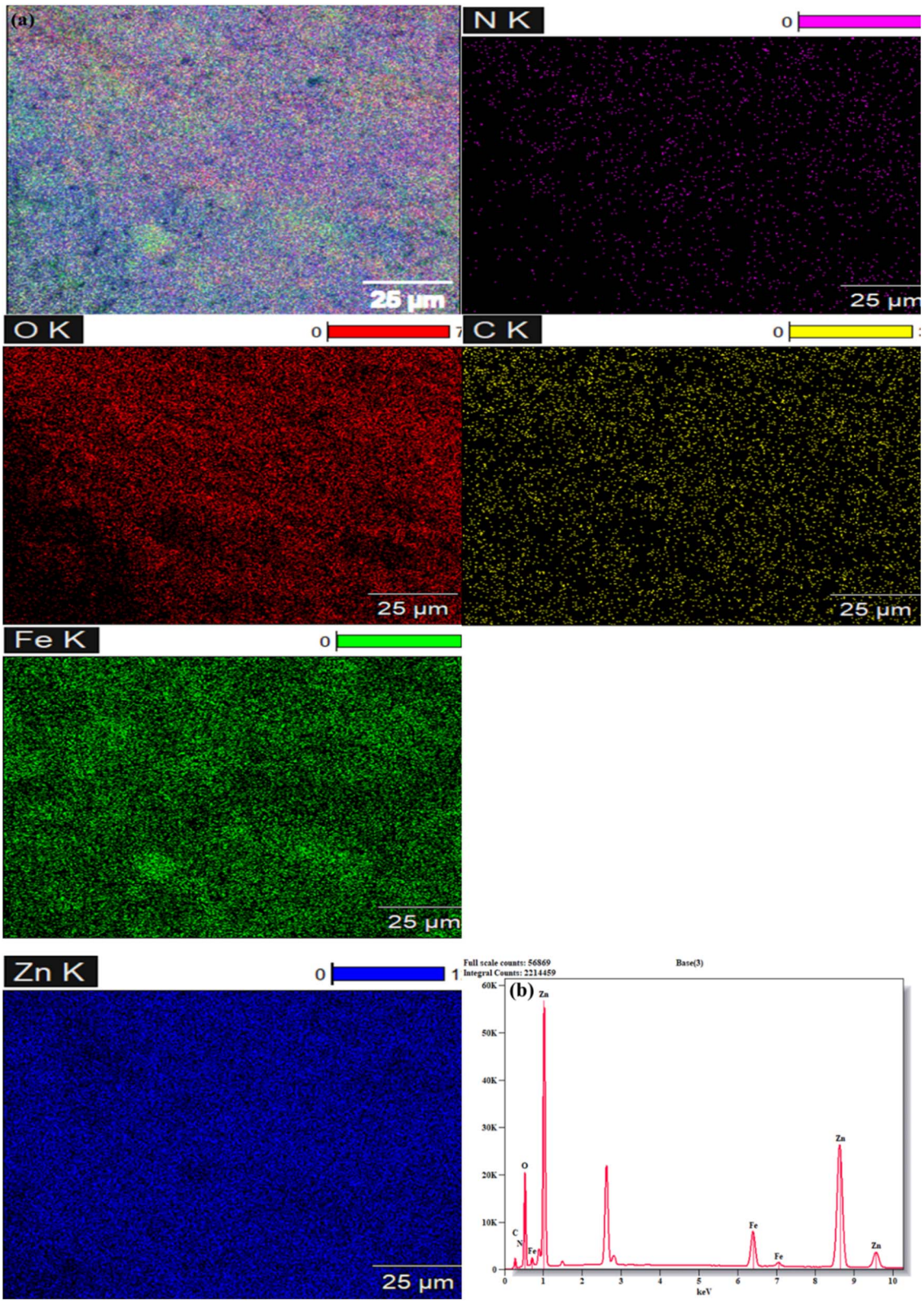

Fig. 4 Mapping of the Lys–Deq/LDH–chia hybrid composite: (a) base image of the material after loading, and (b) corresponding EDX spectrum of the Lys–Deq/LDH–chia.

tend to form larger clusters, reducing the total available surface area. This aggregation reduced surface area due to fewer exposed surfaces.

TGA/DTG was used to examine the thermal behaviour of the LDH–chia hybrid and LDH–chia–Lys–Dqm hybrid composite in order to assess the thermal stability of the manufactured

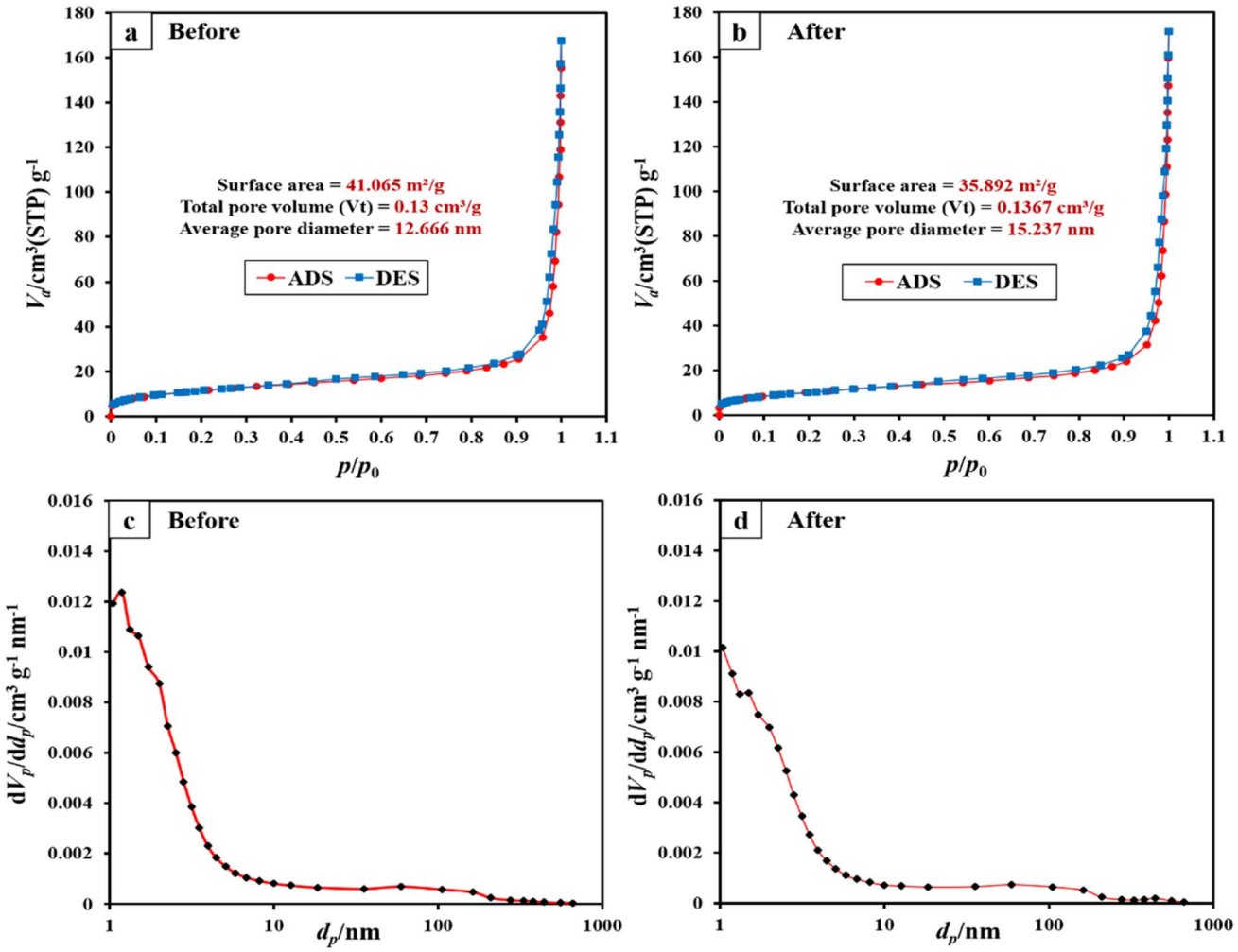

Fig. 5 (a and b) Adsorption–desorption isotherms of N_2 and (c and d) pore diameter distribution curves for the various samples under study.

materials. As shown in Fig. 6(a) at different temperature ranges, the TGA thermogram shows three weight loss events that are typical of LDH materials (based on DTG curve Fig. 6(b)). The loss of physiosorbed surface water molecules is linked to the initial weight loss, which happens between 50 and 250 °C. The decarboxylation of nitrate anions, which causes the layered structure to collapse and interlayer anions to be removed, is responsible for the second weight loss, which takes place between 250 and 400 °C and the weight loss below 400 °C. These results confirmed by the DTG curve that shows two distinct peaks, indicating a multi-step thermal degradation process. One peak around 150 °C and other around 450 °C.

As illustrated in Fig. 6c, the drug elimination in the LDH–chia–Lys–Dqm hybrid composite was observed at the 150–250 and 550–700 °C ranges, respectively. The main reason for the more noticeable increase in the drug elimination range at higher temperatures is the LDH intercalation with regard to free drug. This could be due to the drug's chemical interaction with the LDH within the surfaces. This is further supported by the FTIR and XRD data. 150–250 °C was the temperature range used to remove water, while 550–700 °C was the temperature range used to remove CO_2. This showed improved drug intercalation and thermal stability. Also, the DTG curves confirm the intercalation and thermal stability that appear at peaks around 230 °C and 500 °C (Fig. 6 d).

3.3 Drug release and kinetics

Fig. 7 illustrates the cumulative release percentages of encapsulated and free forms of lysozyme and dequalinium over a 24-hour period. Initially, the free forms of both lysozyme and dequalinium exhibit a rapid release, reaching 50.5 ± 2.12% and 51.11 ± 3.56% respectively within the first 15 minutes, and nearly complete release (99 ± 1.79% and 100 ± 1.18%) by the 2-hour mark. In contrast, the encapsulated forms demonstrate a more controlled and sustained release profile. Where the encapsulated lysozyme releases only 14.5 ± 3.45% in the first 15 minutes, gradually increasing to 91 ± 2.47% by 24 hours, while encapsulated dequalinium shows a similar trend, starting at 15.11 ± 3.68% and reaching 95.56 ± 1.10% at 24 hours. The significant delay in release observed for the encapsulated forms, compared to the rapid release of the free forms, is largely attributed to the properties of the Zn–Fe LDH–chia seed hybrid

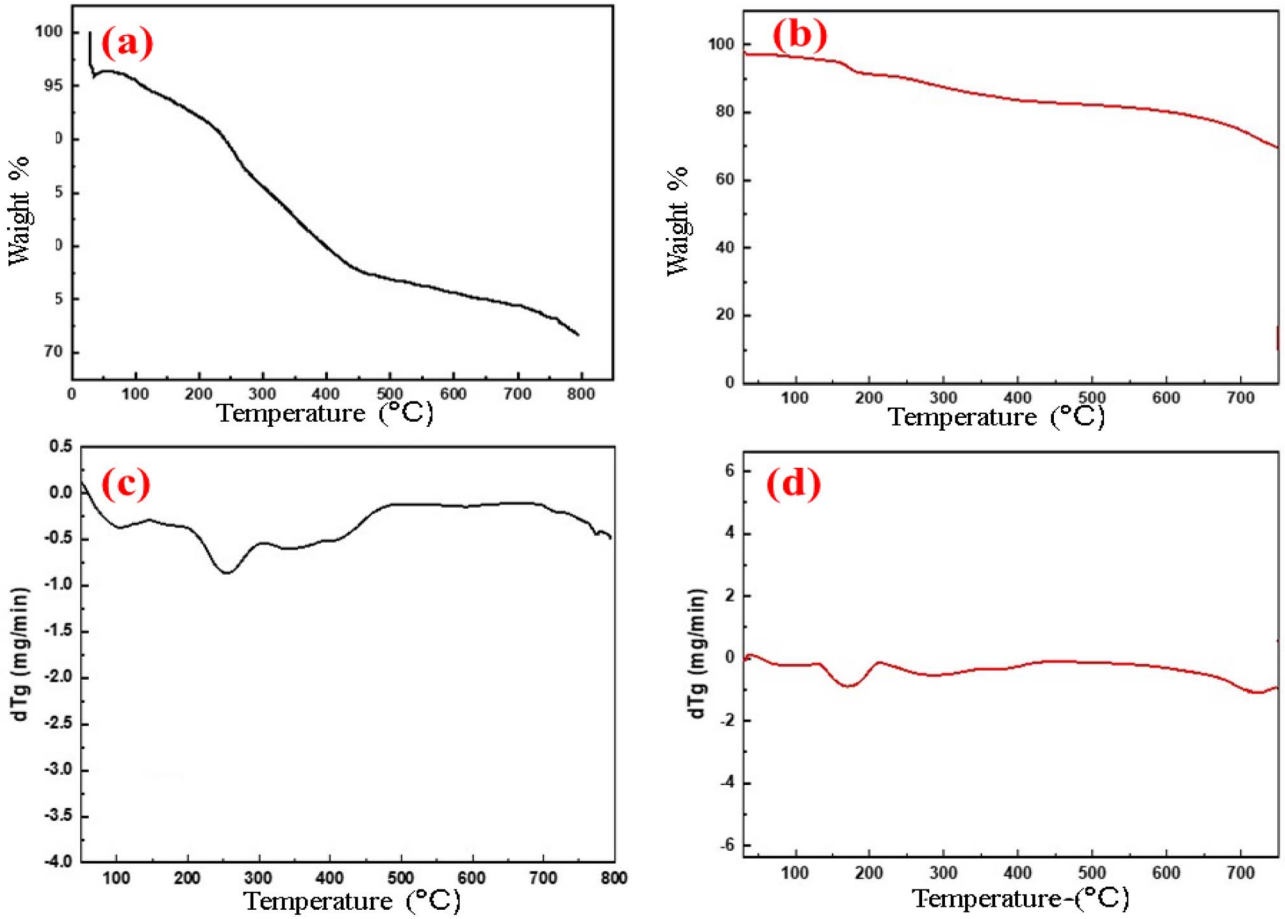

Fig. 6 TGA/DTG thermograms of (a and b) LDH–chia hybrid and (c and d) LDH–chia–Lys–Dqm hybrid composite.

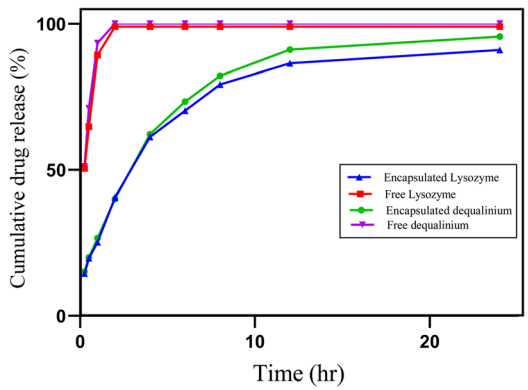

Fig. 7 Cumulative drug release (%) *vs.* time intervals for encapsulated and unencapsulated formulations in Phosphate-Buffered Saline (PBS of pH 6.8).

matrix. Specifically, the polysaccharide-rich chia seed mucilage forms a dense, gel-like network that acts as a hydrophilic diffusion barrier. This network, composed of arabinose, xylose, and glucose units, interacts with both the LDH layers and the encapsulated agents through hydrogen bonding and electrostatic interactions. These interactions stabilize the matrix and hinder the free diffusion of bioactive compounds into the surrounding medium, effectively prolonging their release. The marked difference between the initial burst release of free dequalinium (51.11 ± 3.56% in the first 15 minutes) and that of encapsulated dequalinium (15.11 ± 3.68%) can be explained by several physicochemical features of the LDH–chia matrix including physical diffusion barrier where The layered structure of LDH creates a tortuous and extended pathway that increases the diffusion distance for drug molecules. This effectively slows down the release rate by impeding direct diffusion into the surrounding medium, also since dequalinium, a dicationic molecule with quaternary ammonium groups, forms strong electrostatic bonds with the negatively charged LDH layers. These interactions help retain the drug within the matrix and delay its release. Unlike simple surface adsorption, dequalinium becomes intercalated between the LDH layers during encapsulation. This embedding shields the molecules from immediate contact with the medium, reducing their availability for rapid release. Additionally, chia-derived chitin oligomers within the composite may temporarily lower dequalinium's effective solubility. This occurs *via* hydrogen bonding and hydrophobic interactions, contributing to the slower release profile. Upon hydration, the LDH–chia matrix gradually swells, which regulates water ingress and subsequently controls the drug's dissolution and diffusion during the early release phase.

Together, these mechanisms synergistically suppress the initial burst typically seen in free drug formulations. This controlled release is crucial for dental applications, where sustained antimicrobial activity is required to combat biofilm formation and bacterial colonization over extended periods.[59,60] The encapsulated forms' ability to maintain therapeutic concentrations over time enhances their efficacy in preventing dental caries and periodontal diseases, compared to the rapid depletion observed with free forms.[59,61] This sustained release mechanism not only improves the therapeutic outcomes but also reduces the frequency of application, making encapsulated formulations superior for dental applications.

Table 4 provides a detailed comparison of the release kinetics of encapsulated and unencapsulated lysozyme and dequalinium, key active ingredients in dental therapeutic applications, evaluated using four models: zero-order, first-order, Korsmeyer–Peppas, and Higuchi. The encapsulated forms consistently outperform their unencapsulated counterparts across all models. In the zero-order model, encapsulated lysozyme and dequalinium exhibit higher release rates (encapsulated lysozyme: $K_0 = 12.825 \pm 1.28$, unencapsulated: $K_0 = 4.712 \pm 0.47$), indicating a more controlled and sustained release ideal for long-term dental applications.[62] The first-order model reveals higher K values for encapsulated forms (encapsulated lysozyme: $K = 0.017 \pm 0.002$, unencapsulated: $K = 0.0011 \pm 0.0002$), suggesting efficient release profiles beneficial for rapid and sustained antimicrobial action.[62] The Korsmeyer–Peppas model provides particularly valuable insights into the underlying release mechanisms. Encapsulated formulations demonstrate release exponents approaching anomalous transport (encapsulated lysozyme: $n = 0.478 \pm 0.052$, dequalinium: $n = 0.4519 \pm 0.050$), indicating a balanced release mechanism where both diffusion and polymer relaxation contribute to the controlled delivery.[63] This anomalous (non-Fickian) behavior is likely driven by a synergistic interplay between matrix swelling and drug dissolution. Upon hydration, the chia seed mucilage component gradually swells, increasing the polymeric network's porosity and enabling water ingress. This facilitates both relaxation of the hydrophilic polysaccharide matrix and diffusion of the lysozyme from within the Zn–Fe LDH layers. The lysozyme is thus released through a dual mechanism: one governed by dissolution from the intercalated LDH layers and the other by diffusion through the expanding gel-like mucilage. This combination explains the non-Fickian kinetics observed and supports the suitability of the matrix for sustained oral delivery. In contrast, unencapsulated forms show significantly lower exponents (lysozyme: $n = 0.135 \pm 0.018$, dequalinium: $n = 0.125 \pm 0.018$), typical of rapid dissolution-dominated release that lacks the sustained therapeutic effect necessary for dental applications. The Higuchi model, which specifically characterizes Fickian diffusion processes, further elucidates the role of the LDH–chia matrix in modulating release kinetics. The model fit shows notably higher correlation for encapsulated forms ($R^2 = 0.859$) compared to free forms ($R^2 = 0.330$), confirming that matrix-mediated diffusion is indeed the rate-limiting step in encapsulated formulations. The differing Higuchi constants between encapsulated ($K_H = 94.748 \pm 8.20$) and unencapsulated lysozyme ($K_H = 128.05 \pm 10.90$) quantitatively demonstrate the barrier effect of the LDH–chia matrix.[64] Interestingly, the K_H value for encapsulated lysozyme significantly exceeds that of encapsulated dequalinium ($K_H = 11.106 \pm 1.23$). This variation can be attributed to physicochemical differences between the molecules. Lysozyme is a larger protein (14.3 kDa) with a lower charge density, while dequalinium is a smaller, highly cationic molecule (456 Da) bearing two quaternary ammonium groups. The high charge density of dequalinium facilitates stronger electrostatic binding to the negatively charged LDH layers, resulting in deeper intercalation and slower diffusion through the matrix. Conversely, lysozyme interacts more moderately, allowing it to diffuse more readily through the swollen mucilage network. These contrasting release behaviors highlight the interplay of molecular size, shape, and charge in modulating drug release from hybrid matrices. Based on these parameters, we estimate that the apparent diffusion coefficient for encapsulated active ingredients is approximately two orders of magnitude lower than their free counterparts, which can be directly attributed to three key characteristics of the LDH–chia matrix including tortuous diffusion pathways created by the layered LDH structure, electrostatic interactions between the positively charged active ingredients and negatively charged LDH layers, and hydrogen bonding interactions with chitin oligomers within the matrix.

These mathematical analyses collectively confirm that the sustained release behavior observed in Fig. 8, where encapsulated lysozyme reaches $91.00 \pm 2.47\%$ over 24 hours compared to free lysozyme achieving $99 \pm 1.79\%$ in just 2 hours, is directly attributable to the physicochemical properties of the LDH–chia matrix. The results demonstrate the superiority of the

Table 4 Kinetic parameters for encapsulated and unencapsulated lysozyme and dequalinium[a]

		Active ingredients			
Release kinetic model	Parameters	Encapsulated lysozyme	Unencapsulated lysozyme	Encapsulated dequalinium	Unencapsulated dequalinium
Zero-order model	K_0	12.825 ± 1.28	4.712 ± 0.47	0.713 ± 0.07	0.217 ± 0.02
First-order model	K	0.017 ± 0.002	0.0011 ± 0.0002	0.014 ± 0.0012	0.00046 ± 0.00005
Korsmeyer–Peppas	K	0.281 ± 0.028	0.750 ± 0.56	0.289 ± 0.025	0.776 ± 0.082
model	n	0.478 ± 0.052	0.135 ± 0.018	0.4519 ± 0.050	0.125 ± 0.018
Higuchi model	K_H	94.748 ± 8.20	128.05 ± 10.90	11.106 ± 1.23	14.608 ± 1.56

[a] Data are expressed as means $\pm$ SE (mean $\pm$ SE, $n = 3$).

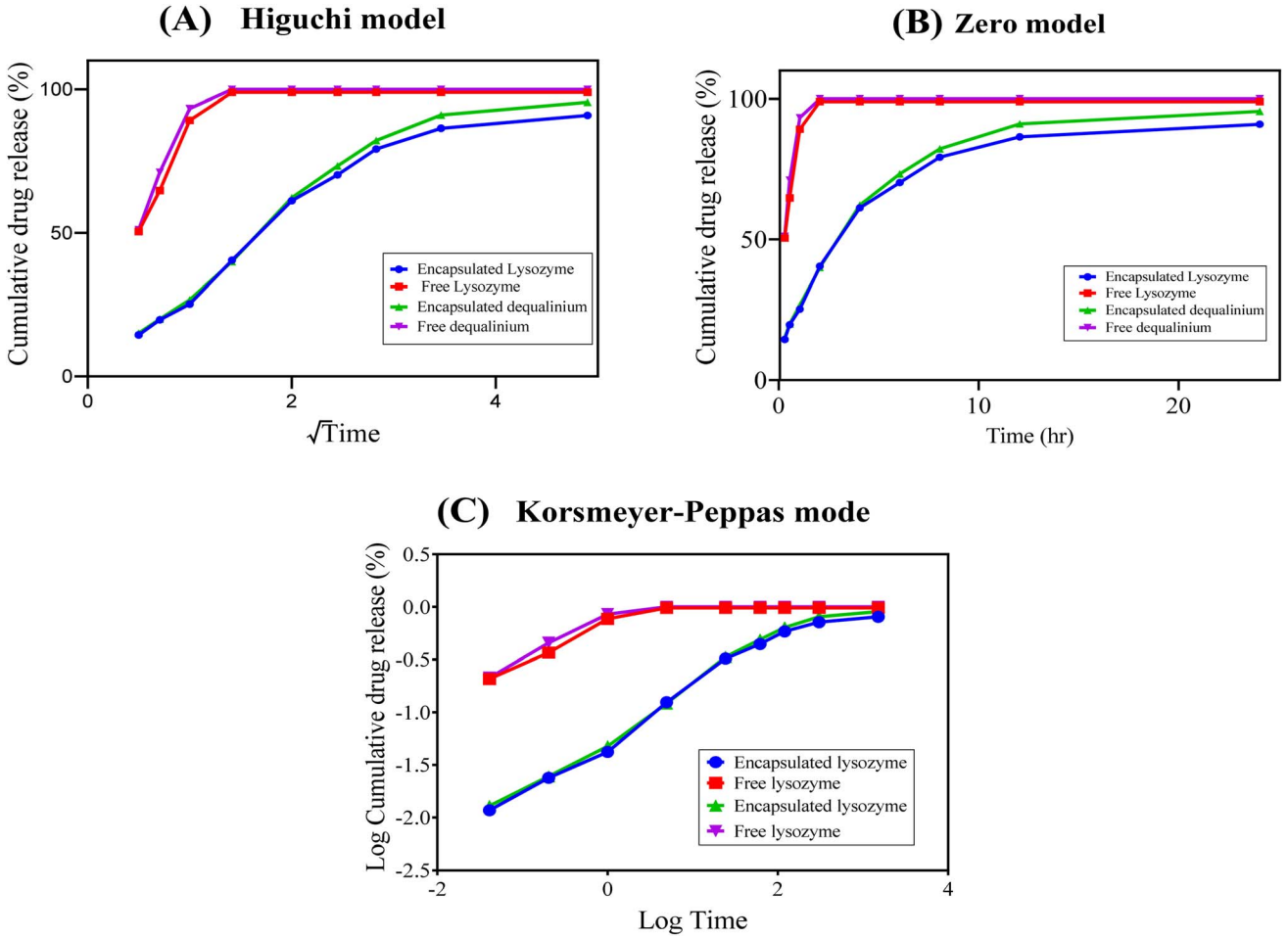

Fig. 8 Drug release kinetics of encapsulated and free lysozyme and dequalinium including Higuchi model (A) that indicates diffusion-controlled release, zero-order model (B) that shows sustained release for encapsulated drugs. (C) Korsmeyer–Peppas model that suggests a non-Fickian diffusion mechanism for encapsulated formulations.

encapsulated forms in release kinetics, offering sustained, efficient, controlled, and steady release, making them more suitable for maintaining therapeutic concentrations against biofilm-forming bacteria in dental applications.

3.4 Antimicrobial efficacy

3.4.1 Zone of inhibition and MIC/MBC analysis. The results of this study demonstrated that all tested materials exhibited antibacterial activity, albeit at varying levels, as shown in Table 5 and Fig. 9–11. Chia seeds showed no significance among the tested microbes in the values of inhibition zone with somewhat comparable values between both Gram positive and Gram-negative bacteria (Fig. 11A). Whereas, testing the antimicrobial potency of Zn Fe LDHs, revealed that *E. coli* represented a wider inhibition zone indication (14.0000 ± 3.2146 mm) (Fig. 11B). Also, the encapsulating formula showed

Table 5 Zone of inhibition of the tested chemicals among strains of Gram negative and Gram-positive bacteria[a]

	Zone of inhibition (mm)			
Strains	Chia seeds	Zn Fe LDHs	Encapsulated formula	Ciprofloxacin
E. coli	7.00 ± 1.73	14.0000 ± 3.2146	16.33 ± 2.33*	7.930 ± 0.764
P. aeruginosa	6.33 ± 2.03	10.3333 ± 1.6667	16.67 ± 2.31	6.432 ± 1.112
K. pneumonia	6.00 ± 2.31	9.6667 ± 4.7022	20.33 ± 2.03*	7.88 ± 0.912
S. aureus	3.67 ± 2.03	9.6667 ± 2.6034*	14.67 ± 0.88**	10.22 ± 0.7542
S. mutans	5.67 ± 1.76	10.6667 ± 0.6667*	24.33 ± 2.03**	9.32 ± 2.134
S. sobrinus	5.34 ± 0.98	8.5342 ± 1.009	11.45 ± 0.887	4.45 ± 0.0971

[a] Data are expressed as means ± SE. *Significant difference at $P < 0.05$, ** significant difference at $P < 0.01$ and ***significant difference at $P < 0.001$.

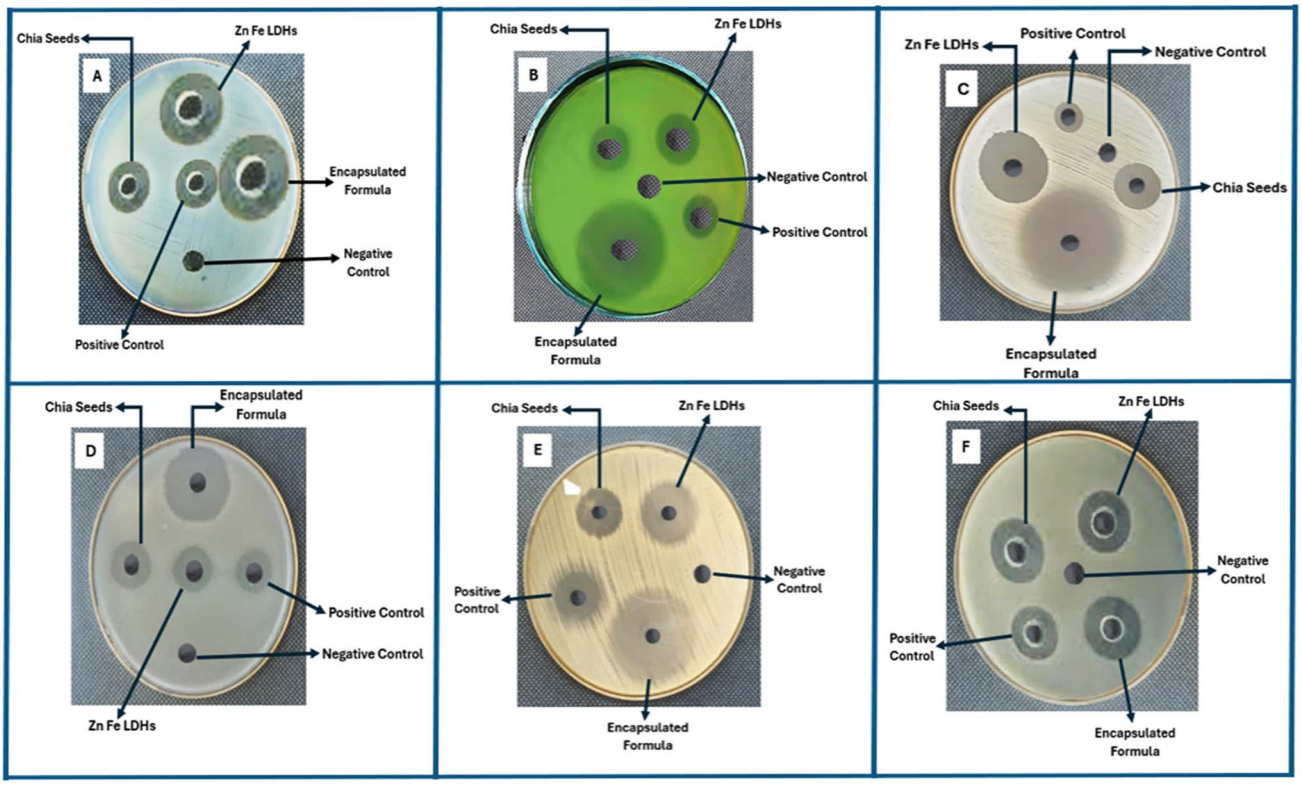

Fig. 9 Zone of inhibition of chia seeds, Zn Fe LDHs-based nanoparticles and encapsulated formula against the tested Gram-positive and Gram-negative bacterial species. A = *E. coli*; B = *P. aeruginosa*; C = *K. pneumoniae*; D = *S. aureus*; E = *S. mutans* and F = *S. sobrinus*.

significant difference for inhibition zone values ($P < 0.01$) against both Gram-positive bacteria, including *S. aureus* (14.67 ± 0.88 mm) and *S. mutans* (24.33 ± 2.03 mm). Additionally, *S. sobrinus* demonstrated a moderate inhibition zone of 11.45 ± 0.887 mm when treated with the encapsulated formula, showing intermediate susceptibility compared to other Gram-positive bacteria tested. Among Gram-negative bacteria, *K. pneumoniae* displayed the broadest inhibition zone (20.33 ± 2.03 mm) at $P < 0.05$, indicating its high susceptibility to the encapsulating formula (Fig. 11B and C).

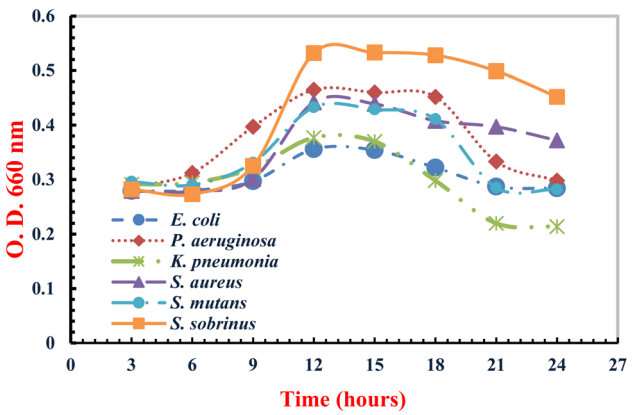

Fig. 10 Growth curves of various bacterial strains treated with encapsulated formula.

As seen from Fig. 10, the encapsulated formula has a stronger inhibitory effect on the growth of the tested pathogens. Sen *et al.*[65–67] stated that cationic peptide crafted from snake venom demonstrated exceptional antibacterial effectiveness against *Escherichia coli*, methicillin-resistant *Staphylococcus aureus* (MRSA), *Pseudomonas aeruginosa*, and *Klebsiella pneumoniae*. The MIC and MBC values (Table 6) revealed that the encapsulating formula required the lowest concentrations to inhibit bacterial growth or achieve complete bacterial killing. Notably, *K. pneumoniae* showed the most significant susceptibility, with an MIC of 13.00 ± 2.60 μg mL^{-1} and an MBC of 20.83 ± 5.23 μg mL^{-1} ($P < 0.001$). *S. mutans* also exhibited high sensitivity, with an MIC of 15.60 ± 1.05 μg mL^{-1} and an MBC of 26.07 ± 5.23 μg mL^{-1} ($P < 0.01$). The MBC/MIC ratio for *S. mutans* was 1.7, indicating a bactericidal effect. *S. sobrinus* showed moderate susceptibility to the encapsulated formula with an MIC of 49.66 ± 4.32 μg mL^{-1} and an MBC of 72.93 ± 6.43 μg mL^{-1}, resulting in an MBC/MIC ratio of 1.47, which suggests a bactericidal effect similar to other tested strains. The relatively low MIC and MBC values suggest that the encapsulating formula is highly effective against Gram-positive bacteria, particularly *S. mutans*.

The findings of this study align with previous research on the antimicrobial properties of chia-based materials. For instance, Motyka *et al.* (2023) reported that chia sprout powders exhibited MIC values ranging from 0.625 to 10 mg mL^{-1} against both Gram-positive and Gram-negative bacteria.[68] Similarly, Abdel-Aty *et al.* (2021) observed MIC values of 0.40–0.65 mg mL^{-1}

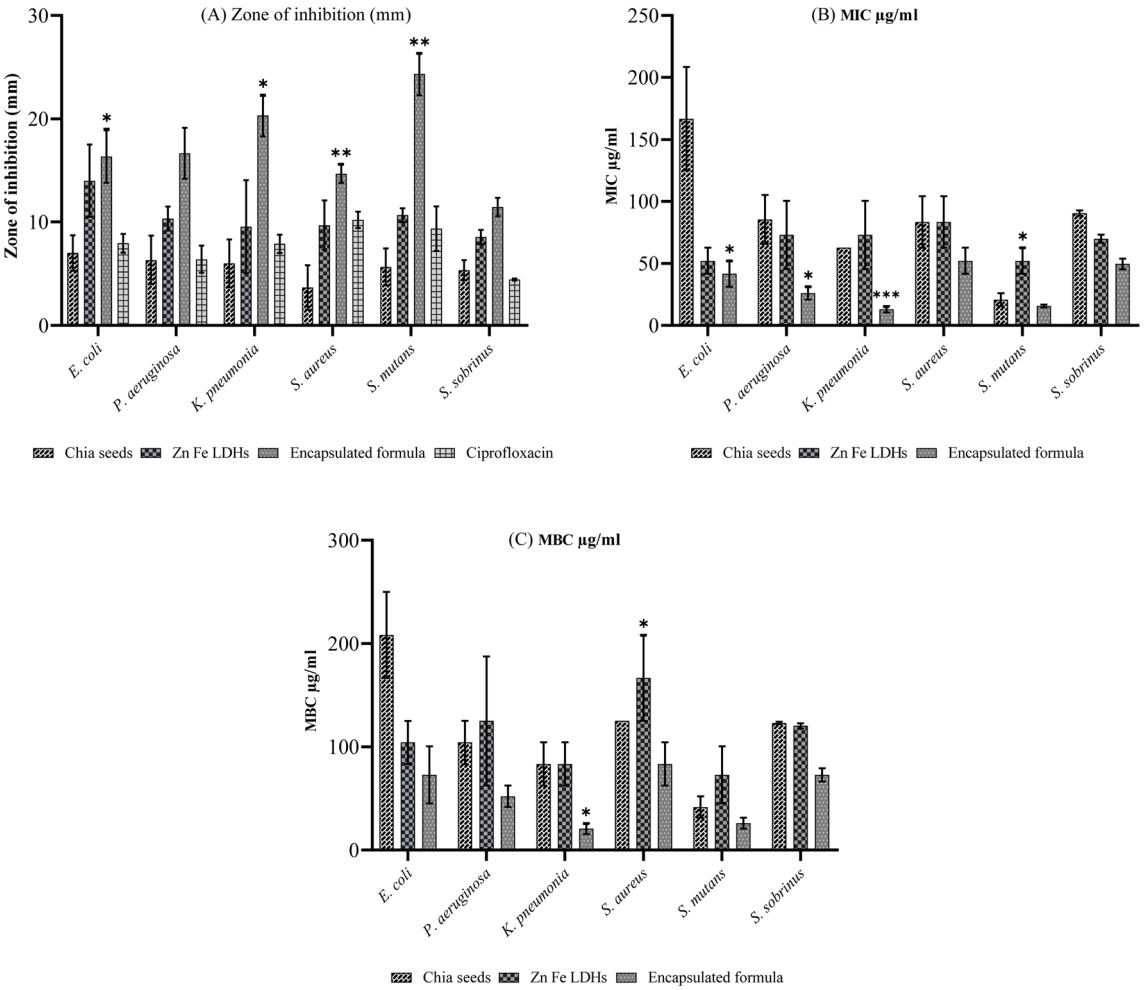

Fig. 11 (A) Zone of inhibition, (B) MICs, and (C) MBCs of chia seeds, Zn Fe LDHs-based nanoparticles and encapsulating formula against the tested Gram-positive and Gram-negative bacterial species.

for chia sprout powders against *E. coli* O157:H7, *S. Typhi*, *P. aeruginosa*, and *S. aureus*.[69] Coelho *et al.* (2018) highlighted that protein hydrolysates in chia seeds had a stronger inhibitory effect against *S. aureus* compared to *E. coli*.[70] Additionally, Krishnappa *et al.* (2017) found that dry chia seed powders exhibited superior antibacterial activity compared to green sprout powders, with MIC values of 3.5 and 4.0 mg mL^{-1} against *S. aureus* and *E. coli*, respectively.[71]

In comparison, chlorhexidine (CHX) is a well-known antibacterial drug in oral health, particularly for its efficacy against a variety of oral infections. Its applications vary from plaque reduction to the prevention of oral illnesses, making it a standard in dentistry. An *in vitro* study showed the antimicrobial activity of 0.2% chlorhexidine mouth rinse against *Staphylococcus aureus*.[72] In another study by Al-Ani *et al.*[73] this study assessed how formulation design affects drug delivery and

Table 6 MICs, MBCs and MBC/MIC ratio of the tested chemicals among strains of Gram negative and Gram-positive bacteria[a]

	Chia seeds (µg mL^{-1})			Zn Fe LDHs (µg mL^{-1})			Encapsulated formula (µg mL^{-1})		
Tested organisms	MIC	MBC	MBC/MIC ratio	MIC	MBC	MBC/MIC ratio	MIC	MBC	MBC/MIC ratio
E. coli	166.67 ± 41.67	208.33 ± 41.67	1.40	52.100 ± 10.400	104.16 ± 20.833	1.90	41.70 ± 10.40*	72.93 ± 27.55	1.60
P. aeruginosa	85.33 ± 19.83	104.17 ± 20.83	1.20	72.93 ± 27.54	125.00 ± 62.500	1.70	26.07 ± 5.23*	52.10 ± 10.40	1.00
K. pneumoniae	62.50 ± 0.00	83.33 ± 20.83	1.30	72.93 ± 27.54	83.33 ± 20.83*	1.10	13.00 ± 2.60***	20.83 ± 5.23*	1.60
S. aureus	83.33 ± 20.83	125.00 ± 0.00	1.50	83.33 ± 20.83*	166.66 ± 41.66*	2.00	52.10 ± 10.40	83.33 ± 20.83	1.50
S. mutans	20.80 ± 5.25	41.63 ± 10.43	2.00	52.100 ± 10.40*	72.93 ± 27.547	1.00	15.60 ± 1.05	26.07 ± 5.23	1.70
S. sobrinus	90.41 ± 2.15	122.92 ± 1.17	1.36	69.74 ± 3.27	120.18 ± 2.43	1.72	49.66 ± 4.32	72.93 ± 6.43	1.47

[a] Data are expressed as means ± SE. *Significant difference at $P < 0.05$, **significant difference at $P < 0.01$ and ***significant difference at $P < 0.001$.

release kinetics of chlorhexidine in mucoadhesive buccal tablets. Using both conventional and novel dissolution methods, the research provided insights into optimizing buccal tablet formulations for effective oral antimicrobial therapy. Also, researchers explored the encapsulation and release of chlorhexidine from cellulose acetate nanofibers. These nanofiber mats demonstrated controlled drug release and effective antibacterial activity against *Streptococcus mutans* and *Enterococcus faecalis*, suggesting potential applications in dental treatments.[74] Furthermore, a study evaluates the antimicrobial activity of chlorhexidine (CHX) in gel form against aspiration pneumonia-inducing bacteria. It compares two gel types containing 1% and 0.1% CHX to a 0.12% CHX solution. The study found that the 1% CHX gels exhibited the highest inhibitory effect on all tested bacteria, particularly *Staphylococcus aureus*. These findings suggest that CHX gels may be a more effective oral care method for hospitalized patients who struggle with using liquid solutions.[75]

Despite the benefits of CHX in eliminating oral pathogens and its effectiveness, it also has several limitations. These include cytotoxicity[76,77] and the development of microbial resistance due to long-term use of CHX. This can lead to reduced bacterial susceptibility and multidrug resistance.[78,79]

On the other hand, the LDH-based components are widely recognized for their antimicrobial properties in various biomedical applications,[80–82] there is a noticeable lack of studies specifically addressing their effectiveness against pathogenic microorganisms in the oral cavity.

Our research focuses on the development of lysozyme–dequalinium–LDH nanocomposites with chia seed mucilage, which combine the beneficial properties of each component. While both lysozyme and LDHs have shown potential for antibacterial activity, the synergistic interactions and amplified effectiveness resulting from their combination have not been thoroughly studied. Additionally, the use of natural components such as lysozyme and chia mucilage may reduce cytotoxicity. Furthermore, the incorporation of LDH structures into a mucoadhesive gel allows for sustained and targeted release, providing prolonged contact with oral biofilm surfaces without systemic exposure. By examining these nanocomposites, our investigation aims to fill the gap in the existing literature and provide valuable insights into their collective antibacterial properties. We hypothesize that the unique physicochemical characteristics of these nanocomposites, including their dimensionality, surface charge, and molecular composition, may lead to enhanced antimicrobial efficacy compared to their individual constituents.

3.4.2 Mechanisms of action and synergistic effects. The lysozyme–dequalinium/Zn–Fe layered double hydroxide (LDH)–chia seed formulation (F3) exhibits superior antimicrobial and

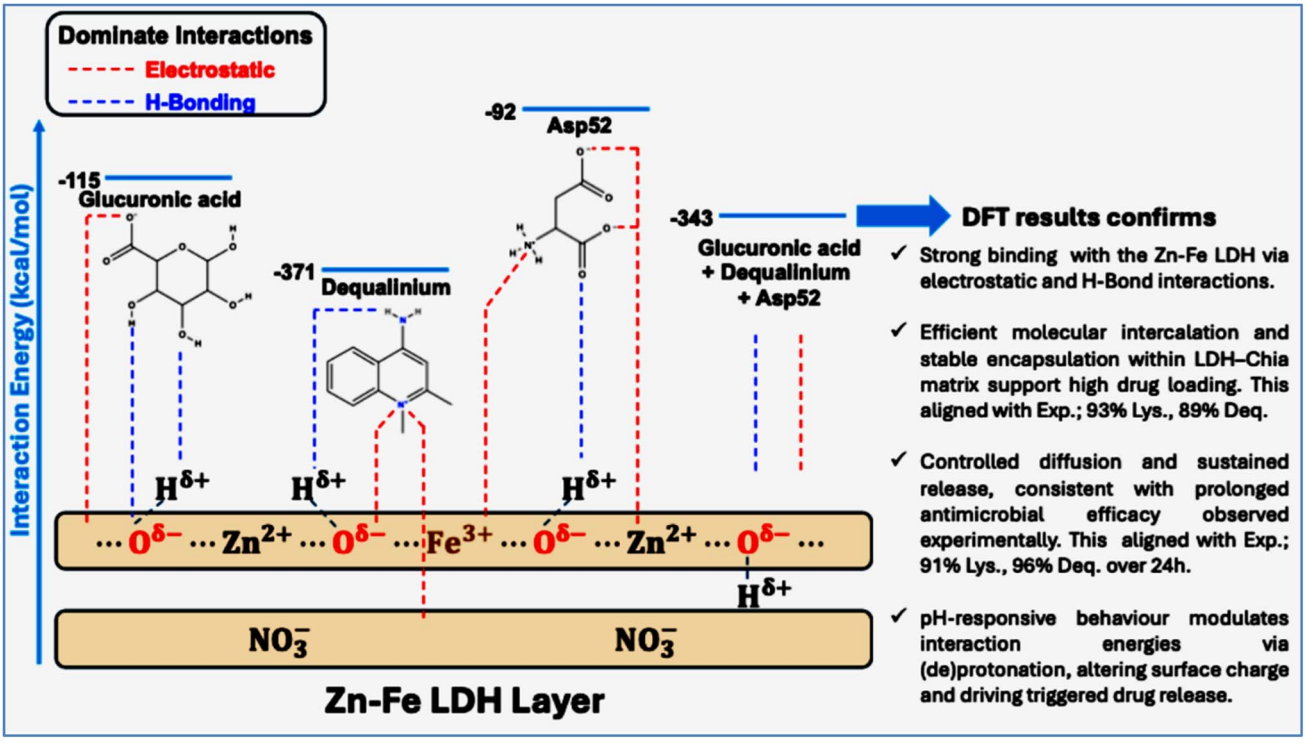

Scheme 2 Schematic representation of DFT-derived molecular interactions within the Zn–Fe LDH–chia seed matrix, integrating computational and experimental insights to highlight sustained release and enhanced antimicrobial efficacy. The Zn–Fe LDH matrix interacts with glucuronic acid (representing chia seed mucilage), Asp52 (modeling lysozyme's active site), and dequalinium cation *via* electrostatic interactions (red dashed lines) and hydrogen bonding (blue dashed lines), with DFT-calculated energies. DFT findings aligned with the experimental results, including encapsulation efficiencies (93.30% lysozyme, 88.74% dequalinium) and sustained release (91% lysozyme, 95.56% dequalinium over 24 h), and underscoring the critical role of pH-dependent protonation/deprotonation of ligands and surface charge variations, on the binding interaction consistent with experimental data.

antibiofilm efficacy (90.1 ± 1.2% *Streptococcus mutans* biofilm inhibition, MIC = 13–15.6 μg mL^{-1}) compared to conventional dental therapies, driven by controlled release, synergistic interactions, and targeted action against oral pathogens. Previous studies have demonstrated the antimicrobial potential of Zn–Fe LDHs, with MIC values of 0.49–15.60 μg mL^{-1} against Gram-positive and Gram-negative bacteria[54] and inhibition zones up to 22 mm against *Escherichia coli*.[83] To elucidate the mechanisms underlying F3's enhanced performance, we conducted a simple DFT study to quantify the adsorption of glucuronic acid (representing chia seed mucilage's polysaccharide component), dequalinium cation, and aspartic acid (Asp52, modeling lysozyme's active site) on a Zn–Fe LDH surface.

3.4.2.1 Release mechanism. The sustained release of lysozyme (91.00 ± 2.47% over 24 hours) and dequalinium (95.56 ± 1.10%), compared to free forms (99–100% in 2 h), is facilitated by strong adsorption within the LDH–chia matrix and effective encapsulation. DFT calculations yield a total interaction energy of −343 kcal mol^{-1} for the full system (glucuronic acid + Asp52 + dequalinium + Zn–Fe-LDH), with pairwise contributions of −115.1 kcal mol^{-1} (glucuronic acid + Zn–Fe-LDH), −370.9 kcal mol^{-1} (dequalinium + Zn–Fe-LDH), and −91.4 kcal mol^{-1} (Asp52 + Zn–Fe-LDH) (Table 2 and Scheme 2). The key interactions include: (a) electrostatic interactions: dequalinium's quaternary ammonium groups interact strongly with LDH's anionic oxygen atoms (CHELPG −0.97*e* on O), contributing to its high binding energy (−370.9 kcal mol^{-1}). Asp52's carboxylate coordinates with LDH's Zn^{2+}/Fe^{3+} (*e.g.*, O···Zn distance of 3.62 Å, CHELPG +1.304095*e* on Zn), stabilizing its adsorption (−91.4 kcal mol^{-1}). (b) Hydrogen bonding: glucuronic acid's hydroxyl/carboxyl groups form H-bonds with LDH's hydroxyls (*e.g.*, O···H distance of 2.48 Å, CHELPG −1.013089*e* on O), supporting its binding (−115.1 kcal mol^{-1}). Asp52's COO^- forms H-bonds with LDH's OH^- (*e.g.*, O···H distance of 2.39 Å, CHELPG −0.90*e* on O). These are corroborated by FTIR peaks at 1745–1460 cm^{-1} (C=O stretching) and 1159.15 cm^{-1} (C–N stretching). (c) Intercalation: XRD reveals a reduced basal spacing (8.88 Å for Lys–Dqm/LDH–chia *vs.* 9.78 Å for LDH), confirming dequalinium and lysozyme intercalation, which extends the diffusion path and enhances stability against environmental stressors.[84]

The Korsmeyer–Peppas model (n = 0.4519–0.478) indicates non-Fickian transport, driven by chia mucilage swelling and drug dissociation from LDH, aligned with strong H-bonding and electrostatic interactions (−343.1 kcal mol^{-1}), as elucidated in Scheme 2. CHELPG analysis suggests glucuronic acid donates slight electron density (~0.75*e*), enhancing matrix stability, though precise charge transfer is limited by fitting challenges in the highly charged system.

Lysozyme and dequalinium in the presence of the LDH carrier. Fig. 12 shows pH-dependent binding energies (E_{int}) calculated for lysozyme and dequalinium in the presence of the LDH carrier. The adsorption energies were calculated across a range of pH values,[1–12] reflecting the protonation and deprotonation dynamics of the drug molecules and the carrier as shown in Fig. 12.

Fig. 12 shows distinct loading and release profiles for both drugs, illustrating how pH changes influence the interaction between the drugs and the LDH carrier. For lysozyme–LDH, the binding energy shows a characteristic V-shaped curve across the pH range, reflecting the drug's ability to interact with the carrier. At pH 1–4, the adsorption energy is relatively high (15.26 kcal mol^{-1}), indicating strong binding between the neutral form of lysozyme and the LDH surface. This behavior is

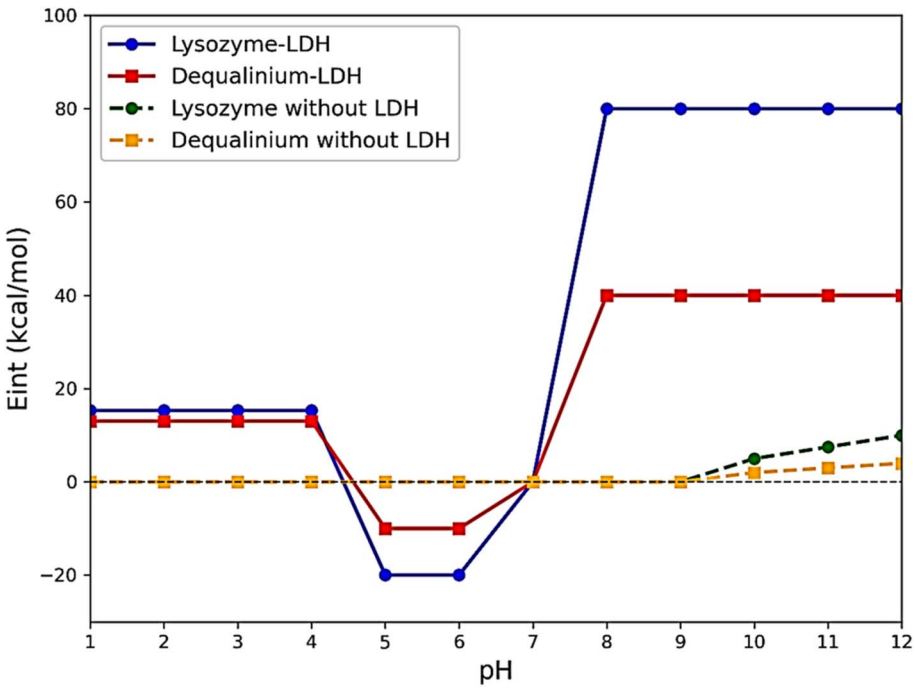

Fig. 12 pH-dependent binding energies (E_{int}) calculated for lysozyme and dequalinium in the presence of the LDH carrier.

expected, as the neutral form of lysozyme is more likely to form stable interactions with the positively charged LDH carrier in this acidic pH range. As the pH increases to 5–6, the binding energy becomes more negative (−20 kcal mol^{-1}), indicating a shift towards drug release. This drop in adsorption energy is attributed to the deprotonation of lysozyme, reducing its electrostatic interaction with the carrier and facilitating its release from the surface. At pH 7, the adsorption energy approaches zero (0 kcal mol^{-1}), indicating no significant interaction between the drug and carrier, which corresponds to the neutral state of both lysozyme and LDH. At pH 8–12, the adsorption energy increases again to positive values (80 kcal mol^{-1}), reflecting the re-adsorption of the deprotonated form of lysozyme to the LDH carrier. This suggests that at higher pH, the lysozyme becomes more negatively charged, leading to a stronger electrostatic attraction with the positively charged LDH surface. This re-adsorption behavior at higher pH is consistent with the expected loading mechanism for lysozyme as the drug undergoes a conformational shift, promoting its interaction with the carrier.

The pH-dependent behavior of dequalinium–LDH follows a similar pattern to lysozyme but with smaller adsorption energies. At pH 1–4, the binding energy is also positive (13 kcal mol^{-1}), indicating moderate adsorption between the neutral form of dequalinium and the LDH surface. However, the adsorption is weaker compared to lysozyme, reflecting the differences in the molecular size and charge distribution between the two drugs. At pH 5–6, the adsorption energy drops to negative values (−10 kcal mol^{-1}), signaling the beginning of drug release due to the deprotonation of dequalinium. Similar to lysozyme, this deprotonation leads to weaker interactions with the carrier, resulting in the release of the drug. The energy reaches zero at pH 7, indicating no significant interaction between the neutral species of both dequalinium and the LDH surface. At pH 8–12, the adsorption energy increases again, but only slightly (40 kcal mol^{-1}), indicating re-adsorption of the deprotonated form of dequalinium to the carrier. The magnitude of the binding energy in this pH range is smaller than that for lysozyme, suggesting a weaker re-adsorption affinity for dequalinium, which is consistent with its smaller molecular size and charge.

For both drugs without the LDH carrier, the adsorption energies are zero for the pH range 1–9, indicating no significant interaction with the surface. This suggests that both lysozyme and dequalinium exist primarily in their neutral or weakly protonated forms within this pH range, which are not conducive to strong binding or adsorption. As the pH increases beyond pH 9, the adsorption energies for both drugs increase slightly, with lysozyme reaching a maximum of 10 kcal mol^{-1} at pH 12, and dequalinium reaching 4 kcal mol^{-1}. These slight increases reflect the minor adsorption that occurs as the drugs become more deprotonated at higher pH, but the interaction is still much weaker compared to when they are in the presence of the LDH carrier.

3.4.2.2 Mechanisms of loading and release

3.4.2.2.1 Loading mechanism. The results suggest that lysozyme and dequalinium both exhibit efficient loading at lower pH,[1–4] where the neutral forms of the drugs interact strongly with the positively charged LDH carrier. The adsorption energy for both drugs is positive, indicating that the drugs are stably bound to the carrier surface at this pH range.

3.4.2.2.2 Release mechanism. As the pH increases,[5–7] both drugs undergo protonation/deprotonation changes, which weaken their interactions with the carrier. This is reflected by the negative adsorption energies in the pH range 5–6, indicating the release of the drug from the carrier. This release is more prominent for lysozyme, which exhibits a larger negative shift in adsorption energy compared to dequalinium.

3.4.2.2.3 Re-adsorption at high pH. At pH 8–12, both drugs show re-adsorption to the carrier, as the deprotonated forms of the drugs interact more strongly with the positively charged LDH surface. However, the binding strength at higher pH is still weaker than at lower pH, particularly for dequalinium, which has a smaller increase in adsorption energy compared to lysozyme.

3.4.2.3 Synergistic effects. The formulation's bactericidal activity (MBC/MIC < 4)[85] results from synergistic interactions among its components, combining computational and biological mechanisms: lysozyme: computationally treated as Asp52 which hydrolyzes bacterial peptidoglycan, with stable LDH binding (−91.4 kcal mol^{-1}) *via* H-bonds (2.39 Å) and COO^- coordination (3.62 Å). Biologically, lysozyme's constituents (ovotransferrin, albumin, avidin, ovomucoid) provide intracellular defense against microbes.[86] Dequalinium: it exhibits strong intercalation (−370.9 kcal mol^{-1}) driven by electrostatic interaction. As a lipophilic bis-quaternary ammonium compound, it disrupts mitochondrial DNA, enzymes, and energy production, leading to cell death.[87–89] Chia mucilage: computationally treated as glucuronic acid, which provides mucoadhesion and drug protection (−115.1 kcal mol^{-1}) *via* H-bonds (2.48 Å). Its bioactive compounds (linolenic/linoleic acids, omega-3, quercetin, kaempferol, caffeic acid, *p*-coumaric acid) inhibit bacterial enzymes and disrupt cellular functions.[90–92] Finally, Zn–Fe LDH which can release Zn^{2+} for reactive oxygen species (ROS) generation, inducing enzymatic inhibition, protein degradation, and membrane lysis without adverse effects on host cells.[93,94] The total interaction energy (−343.1 kcal mol^{-1}) is less negative than the sum of pairwise interactions (−577.4 kcal mol^{-1}), indicating cooperative effects that enhance matrix stability and antimicrobial efficacy through controlled release and synergy (Table 2 and Scheme 2).

3.4.2.4 Targeted action mechanism. The formulation targets oral pathogens and biofilms through:

(a) Mucoadhesion: the + 26.44 mV zeta potential ensures electrostatic adhesion to bacterial surfaces, prolonging contact and achieving 90.1% *S. mutans* inhibition.

(b) Biofilm disruption: lysozyme degrades extracellular polymeric substance (EPS), dequalinium targets embedded bacteria, and Zn^{2+} destabilizes EPS *via* ROS, supported by strong adsorption (−343.1 kcal mol^{-1}).

(c) Nanostructure: FESEM reveals a 3D networked morphology (237 nm, 15.23 nm pores), enhancing penetration (surface area 35.892 m^2 g^{-1}).

These findings, integrating calculations results, and experimental data, supported by prior studies,[54] provide a comprehensive mechanistic framework for F3's sustained, targeted antimicrobial action, surpassing conventional dental therapies.

3.4.3 Mechanisms of action and synergistic effects. The antimicrobial efficacy of Zn–Fe layered double hydroxides (LDHs) has also been well-documented. Moaty *et al.* (2016) reported MIC values of Zn–Fe LDHs ranging from 0.49 to 15.60 μg mL^{-1} against various Gram-positive and Gram-negative bacteria.[54] Abdel Aziz *et al.* (2023) further emphasized the antimicrobial potential of Zn–Fe LDHs against *S. agalactiae* and *S. aureus* for wastewater decontamination.[81] Elkartehi *et al.* (2023) demonstrated that a Zn–Fe LDH-zeolite composite at 1000 μg mL^{-1} produced a 22 mm inhibition zone against *E. coli*.[83] The antibacterial activity of the tested materials can be attributed to several mechanisms. Chia seeds contain linolenic acid, linoleic acid, and antioxidants such as omega-3 fatty acids, which contribute to their antimicrobial properties.[90,91] Additionally, bioactive compounds like quercetin, kaempferol, caffeic acid, and *p*-coumaric acid in chia seeds inhibit bacterial enzymes and disrupt cellular functions.[92] Using lysosomes derived from poultry egg white in the encapsulating formula, demonstrated an intracellular defense mechanism towards an array of microbes through their biological constituents, including ovotransferrin, albumin, avidin, and ovomucoid, which improved the powerful antimicrobial effects.[86] Additionally, dequalinium chloride is a lipophilic bis-quaternary ammonium compound is a main component of the encapsulating formula that possesses two positive localized charges it can interact with cellular structures that contain nucleic acids and the mitochondrial membrane.[87,88] It is linked to the depletion of mitochondrial DNA and enzymes as well as the inhibition of cell energy production, which terminates in the death of cells.[89] Similarly, Zn–Fe LDH nanoparticles induce enzymatic inhibition and protein degradation, leading to bacterial cell death and membrane lysis without adverse effects on host cells.[93,94] The encapsulating formula demonstrated a high degree of synergistic bactericidal activity. The encapsulation of chia seeds effectively captured and released the active compounds in a controlled manner, enhancing their stability against environmental stressors.[84] Notably, the formulation exhibited significant antimicrobial activity against *Streptococcus sobrinus*, achieving an MIC of 2.25 μg mL^{-1} and a 17 mm inhibition zone at 1000 μg mL^{-1}, confirming its potent efficacy against this cariogenic bacterium. Furthermore, the MBC/MIC ratio for all tested chemicals was less than 4, indicating bactericidal effects against the examined bacterial species.[68,85,95]

3.4.4 Antibiofilm activity. The results, as presented in Table 7 and Fig. 13 reveal significant differences in biofilm inhibition across the various experimental treatments. Tubes without any synthesized agents (control group) exhibited substantial biofilm growth. This was confirmed by the presence of a thick, whitish-yellow layer at the air-liquid interface and intense blue staining with crystal violet. Tubes treated with Zn–Fe LDH–chia seed hybrid formulations (F1, F2, F3) showed a marked reduction in biofilm formation. F3 (15%) demonstrated the highest efficacy, reducing biofilm formation by 90.1 ± 1.2%. F2 (10%) and F1 (5%) also showed significant inhibition, reducing biofilm formation by 75.8 ± 1.8% and 60.3 ± 2.5%, respectively, compared to the control group. Similarly, against *S. sobrinus*, the hybrid formulations exhibited concentration-dependent biofilm inhibition. F3 (15%) achieved the highest inhibition at 80.5 ± 1.32%, followed by F2 (10%) with 63.0 ± 0.943% inhibition, and F1 (5%) with 51.2 ± 0.971% inhibition. While the inhibition percentages for *S. sobrinus* were slightly lower than those observed for *S. mutans*, the trend remained consistent, demonstrating the broad-spectrum antibiofilm activity of the hybrid formulations. Optical density (OD)

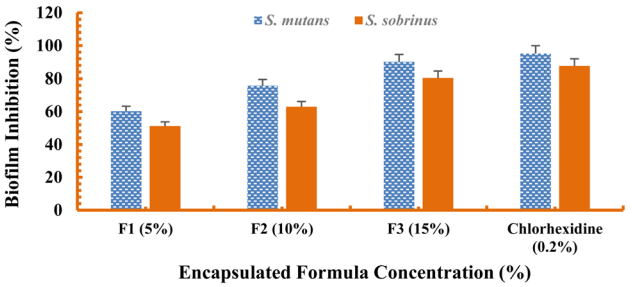

Fig. 13 Percentage of biofilm inhibition by *S. mutans* and *S. sobrinus* for different concentrations of Zn–Fe LDH–chia seed hybrid formulations compared to chlorhexidine (0.2%). F1 (5%), F2 (10%), and F3 (15%) represent Zn–Fe LDH–chia seed hybrid formulations with 5%, 10%, and 15% active material concentrations, respectively. Both *S. mutans* and *S. sobrinus* showed concentration-dependent inhibition, with *S. mutans* demonstrating higher susceptibility to the hybrid formulations. Data are expressed as means ± SE ($n = 3$). Statistical significance was determined using one-way ANOVA followed by Tukey's *post-hoc* test.

Table 7 The percentage of biofilm inhibition for each formulation compared to the control[a]

	OD of crystal violet stain at 570.0 nm					Inhibition%			
			Zn–Fe LDH–chia seed hybrid formulations			Zn–Fe LDH–chia seed hybrid formulations			
Tested organism	Control (untreated)	Chlorhexidine (0.2%)	F1 (5%)	F2 (10%)	F3 (15%)	F1 (5%)	F2 (10%)	F3 (15%)	Chlorhexidine (0.2%)
S. mutans	1.2 ± 0.2	0.030 ± 0.008	0.370 ± 0.025	0.190 ± 0.018	0.060 ± 0.012	60.3 ± 2.5%	75.8 ± 1.8%	90.1 ± 1.2%	95.2 ± 0.8%
S. sobrinus	1.5 ± 0.07	0.186 ± 0.042	0.732 ± 0.173	0.555 ± 0.221	0.292 ± 0.324	51.2 ± 0.971	63.0 ± 0.943	80.5 ± 1.32	87.6 ± 0.97

[a] Data are expressed as means ± SE.

measurements at 570 nm further supported these findings. A significant decrease in OD570 values was observed for tubes treated with F1, F2, and F3 against both *S. mutans* and *S. sobrinus*, indicating a lower amount of crystal violet-stained biofilm. For *S. mutans*, the OD values decreased from 1.2 ± 0.2 (control) to 0.060 ± 0.012 (F3), while for *S. sobrinus*, the values decreased from 1.5 ± 0.07 (control) to 0.292 ± 0.324 (F3). The deep blue color observed after crystal violet staining and ethanol powder visually confirmed the level of biofilm accumulation.

The results demonstrated a clear concentration-dependent relationship, with higher concentrations of the synthesized materials (F3 > F2 > F1) leading to greater biofilm inhibition against both bacterial strains. Notably, *S. mutans* appeared more susceptible to the hybrid formulations than *S. sobrinus*, which may be attributed to differences in biofilm matrix composition and structural organization between these two cariogenic bacteria.

In conclusion, the Zn–Fe LDH–chia seed hybrid formulations effectively inhibited biofilm formation by both *S. mutans* and *S. sobrinus*, with F3 showing the highest efficacy against both organisms. The formulations demonstrated superior performance against *S. mutans* compared to *S. sobrinus*, suggesting species-specific variations in biofilm susceptibility. These findings highlight the potential of these hybrid materials as broad-spectrum anti-biofilm agents.

3.4.5 Role of mucoadhesive properties and mechanisms of biofilm inhibition. The mucoadhesive properties of the Zn–Fe LDH–chia hybrid formulation are critically influenced by its positive zeta potential (+26.44 ± 1.21 mV), which enhances electrostatic interactions with the negatively charged biofilm matrix and mucosal surfaces in the oral cavity.[96] This charge-driven adhesion prolongs contact time, allowing sustained antimicrobial activity by maintaining proximity to the biofilm and facilitating deeper penetration of active ingredients into its structure.[97,98] The interaction is consistent with mucoadhesion theories emphasizing the importance of surface charge and hydrophilicity in polymer-mucus binding.[96] In biofilm inhibition, the Zn–Fe LDH–chia formulation demonstrates superior performance against both tested organisms, with F3 achieving 90.1 ± 1.2% inhibition against *S. mutans* and 80.5 ± 1.32% against *S. sobrinus*. The differential efficacy between *S. mutans* and *S. sobrinus* can be attributed to species-specific biofilm architecture and matrix composition. *S. mutans* biofilms are characterized by higher glucan content and denser extracellular polymeric substance (EPS) networks, which may be more susceptible to the hybrid formulation's multi-mechanistic disruption approach. In contrast, *S. sobrinus* biofilms typically exhibit different polysaccharide compositions and structural arrangements, potentially offering greater resistance to certain antimicrobial mechanisms.

The hybrid system outperforms chlorhexidine through multi-mechanistic actions against both bacterial species. While chlorhexidine rapidly disrupts bacterial membranes *via* electrostatic binding and cell lysis (achieving 95.2 ± 0.8% inhibition against *S. mutans* and 87.6 ± 0.97% against *S. sobrinus*), the hybrid system employs a combination of physical biofilm matrix disruption, electrostatic interactions with bacterial surfaces, and potential enzymatic hydrolysis of extracellular polymeric substances (EPS).[99] For example, Zn–Fe LDHs have demonstrated antibiofilm efficacy by destabilizing EPS components like polysaccharides and proteins, as observed in studies on *S. aureus* and *E.coli* biofilms.[81,99] The consistent performance of the hybrid formulations against both *S. mutans* and *S. sobrinus*, despite their distinct biofilm characteristics, suggests that the multi-target approach effectively addresses the diversity in cariogenic biofilm structures. This slower, sustained mode of action reduces the risk of bacterial resistance and ensures prolonged efficacy, a key advantage for dental applications requiring long-term biofilm management.[81] The hybrid formulation's ability to penetrate biofilms is further enhanced by its nanostructured design, which enables adsorption to bacterial surfaces and disruption of metabolic pathways.[100] Such mechanisms align with findings on LDH-based systems that combine metal ion release (*e.g.*, Zn^{2+}) with reactive oxygen species (ROS) generation to impair bacterial viability.[81] The broad-spectrum activity observed against both *S. mutans* and *S. sobrinus* indicates that these mechanisms are effective across different cariogenic bacterial species, supporting the potential for comprehensive oral biofilm management. Compared to chlorhexidine's transient effects, the Zn–Fe LDH–chia system's gradual release of active components supports sustained antimicrobial activity, making it a promising candidate for preventing oral biofilm-related pathologies like plaque and gingivitis.[81,97] The demonstrated efficacy against both major cariogenic bacteria further strengthens its potential as a comprehensive oral care agent (Fig. 13).

3.5 Cytotoxicity assessment

The cytotoxicity evaluation of lysozyme, dequalinium, LDH–chia seed hybrid, and the encapsulated lysozyme–dequalinium/LDH–chia formulation on human gingival fibroblast cells (HGF-1) revealed the superior biocompatibility and therapeutic potential of the encapsulated formulation. With a CC50 value of 306.6 ± 1.16 μg mL^{-1}, the encapsulated formulation demonstrated significantly lower cytotoxicity compared to lysozyme (238.8 ± 2.05 μg mL^{-1}) and dequalinium (200.54 ± 1.86 μg mL^{-1}), while maintaining a favorable safety profile relative to the LDH–chia seed hybrid (427.56 ± 5.36 μg mL^{-1}), as shown in Fig. 14. This indicates that the encapsulation process not only enhances the stability and delivery of the active compounds but also reduces their toxic effects on healthy cells. The encapsulated formulation's balanced cytotoxicity profile positions it as a promising candidate for dental therapeutics, offering an effective and safer alternative for treating oral infections while minimizing harm to surrounding tissues. The inclusion of lysozyme as a comparative component in this cytotoxicity assessment is well-supported by its established role in oral health applications. Lysozyme has been extensively documented for its selective antibacterial properties against oral microorganisms, including *Streptococcus mutans* serotypes, *Veillonella alcalescens*, and *Actinomyces viscosus* strains.[101] As a naturally occurring antimicrobial enzyme present in saliva

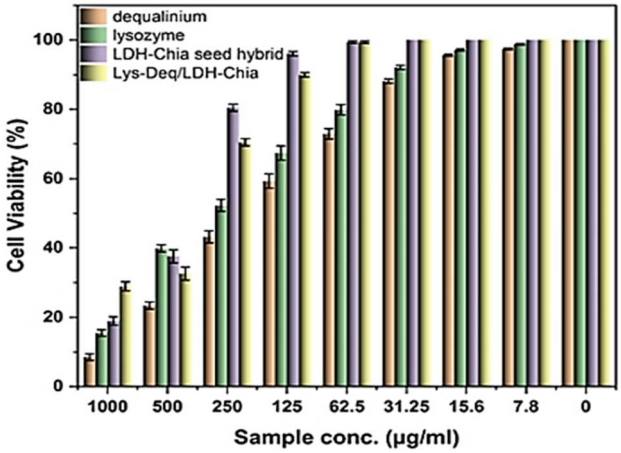

Fig. 14 Cytotoxicity of dequalinium, lysozyme, LDH–chia seed hybrid and Lys–Deq/LDH–chia formulations on Human Gingival Fibroblast cells (HGF-1).

and other mucosal secretions, lysozyme serves as a cornerstone of innate immunity with both direct antimicrobial roles and immune modulation functions.[102] The protein's established biocompatibility and therapeutic potential have been demonstrated in various formulations, where it is often incorporated into 3D hydrogel matrices and oral hygiene products for its antibacterial effects while maintaining cellular compatibility.[103,104] The comparison of individual components (lysozyme and dequalinium) with the encapsulated formulation demonstrates the protective effect of the LDH–chia matrix, evidenced by the improved CC50 value of the encapsulated system compared to free lysozyme, highlighting the enhanced safety profile achieved through our encapsulation technology. These findings underscore the superiority of the encapsulated system in optimizing therapeutic efficacy and biocompatibility for clinical applications.

3.6 Study limitations and future prospects

While this study demonstrates the promising potential of the lysozyme–dequalinium chloride-loaded Zn–Fe LDH–chia seed matrix for enhanced antimicrobial efficacy and sustained drug delivery in dental applications, several limitations should be acknowledged. The experiments were conducted exclusively under *in vitro* conditions, which do not fully replicate the complex oral environment where factors such as enzymatic degradation (including lysozyme stability in saliva), pH fluctuations, and the presence of various ions and organic matter may impact the stability, release profile, and antimicrobial performance of the encapsulated agents. Specifically, the stability of lysozyme in saliva and the structural integrity of the Zn–Fe LDH matrix under varying pH conditions were not directly assessed. Additionally, although the mucoadhesive properties of chia seed mucilage are well-documented, direct experimental evaluation of mucoadhesion was not performed in this study. Future research should therefore focus on comprehensive *in vitro* and *ex vivo* studies simulating the oral environment including exposure to salivary enzymes, dynamic pH conditions, and mechanical forces to assess the formulation's stability, drug release, and antimicrobial efficacy under physiologically relevant conditions. Quantitative mucoadhesion testing, such as texture analyzer-based detachment force measurements or *ex vivo* mucosal retention assays, should be incorporated to confirm and characterize the adhesive performance of the LDH–chia seed matrix. Additionally, future cytotoxicity studies should incorporate established dental antibiotics such as amoxicillin or cephalexin as positive controls alongside our lysozyme-based formulations to provide a more comprehensive comparative framework for clinical translation and better establish the therapeutic positioning of the developed system relative to conventional dental antimicrobial therapies. Furthermore, *in vivo* studies in appropriate animal models or clinical trials will be essential to evaluate the formulation's safety, biocompatibility, and therapeutic efficacy, while exploring the potential for incorporating additional bioactive agents or optimizing the matrix composition may further enhance the system's versatility and effectiveness for targeted dental therapeutics. Although two dental pathogens (*Streptococcus mutans* and *Streptococcus sobrinus*) were included in the anti-biofilm assays, confocal laser scanning microscopy (CLSM) was not performed due to funding constraints. This limitation has been acknowledged, and the authors are currently preparing a follow-up manuscript focused on the same compound, where CLSM-based biofilm imaging will be included as part of the extended investigation.

4 Conclusion

This study highlights the successful development of a lysozyme–dequalinium chloride-loaded Zn–Fe layered double hydroxide (LDH)–chia seed mucilage matrix as a groundbreaking therapeutic system for combating biofilm-associated dental diseases. The optimized formulation achieved high encapsulation efficiency, sustained drug release, and exceptional colloidal stability, addressing the limitations of rapid drug depletion seen in conventional treatments. *In vitro* release studies confirmed a controlled and prolonged release profile for both lysozyme and dequalinium, ensuring long-term therapeutic efficacy. The formulation demonstrated remarkable antimicrobial activity against key pathogens, including *Streptococcus mutans*, *Staphylococcus aureus*, and *Klebsiella pneumoniae*, and *Streptococcus sobrinus* with low minimum inhibitory concentrations (MICs) and MBC/MIC ratios below 4, confirming its potent bactericidal effects. Furthermore, the system exhibited significant antibiofilm activity, effectively reducing *S. mutans* biofilm formation, a critical factor in the progression of dental caries and periodontal diseases. The encapsulated lysozyme–dequalinium/LDH–chia formulation (CC50 of 306.6 μg mL^{-1}) exhibits lower cytotoxicity than its components, demonstrating superior biocompatibility and safety for dental therapeutics. The synergistic interaction between lysozyme, dequalinium chloride, Zn–Fe LDH, and chia seed mucilage not only enhanced antimicrobial and antibiofilm efficacy but also

improved biocompatibility and mucoadhesive properties, making it highly suitable for oral applications.

Conflicts of interest

All authors declare that they have no conflicts of interest to disclose.

Data availability

The datasets used and/or analyzed during the current study available from the corresponding author on reasonable request.

Acknowledgements

This work was supported and funded by the Deanship of Scientific Research at Imam Mohammad Ibn Saud Islamic University (IMSIU) (grant number IMSIU-DDRSP2501).

References

1 N. J. Kassebaum, E. Bernabé, M. Dahiya, B. Bhandari, C. Murray and W. Marcenes, Global burden of untreated caries: a systematic review and metaregression, *J. Dent. Res.*, 2015, **94**(5), 650–658.
2 V. Pérez-Laguna, I. García-Luque, S. Ballesta, L. Pérez-Artiaga, V. Lampaya-Pérez, S. Samper, *et al.*, Antimicrobial photodynamic activity of Rose Bengal, alone or in combination with Gentamicin, against planktonic and biofilm *Staphylococcus aureus*, *Photodiagn. Photodyn. Ther.*, 2018, **21**, 211–216.
3 P. N. Denev, C. G. Kratchanov, M. Ciz, A. Lojek and M. G. Kratchanova, Bioavailability and antioxidant activity of black chokeberry (*Aronia melanocarpa*) polyphenols: in vitro and in vivo evidences and possible mechanisms of action: a review, *Compr. Rev. Food Sci. Food Saf.*, 2012, **11**(5), 471–489.
4 M. D. J. Libardo, A. A. Bahar, B. Ma, R. Fu, L. E. McCormick, J. Zhao, *et al.*, Nuclease activity gives an edge to host-defense peptide piscidin 3 over piscidin 1, rendering it more effective against persisters and biofilms, *FEBS J.*, 2017, **284**(21), 3662–3683.
5 P. Gilbert and L. Moore, Cationic antiseptics: diversity of action under a common epithet, *J. Appl. Microbiol.*, 2005, **99**(4), 703–715.
6 V. Rives, M. Del Arco and C. Martín, Layered double hydroxides as drug carriers and for controlled release of non-steroidal antiinflammatory drugs (NSAIDs): a review, *J. Controlled Release*, 2013, **169**(1–2), 28–39.
7 P. K. Stoimenov, R. L. Klinger, G. L. Marchin and K. J. Klabunde, Metal oxide nanoparticles as bactericidal agents, *Langmuir*, 2002, **18**(17), 6679–6686.
8 Z. P. Xu, Q. H. Zeng, G. Q. Lu and A. B. Yu, Inorganic nanoparticles as carriers for efficient cellular delivery, *Chem. Eng. Sci.*, 2006, **61**(3), 1027–1040.
9 L. A. Muñoz, A. Cobos, O. Diaz and J. M. Aguilera, Chia seeds: Microstructure, mucilage extraction and hydration, *J. Food Eng.*, 2012, **108**(1), 216–224.
10 S. E. Carone, T. R. Costa, S. M. Burin, A. C. Cintra, K. F. Zoccal, F. J. Bianchini, *et al.*, A new l-amino acid oxidase from Bothrops jararacussu snake venom: Isolation, partial characterization, and assessment of pro-apoptotic and antiprotozoal activities, *Int. J. Biol. Macromol.*, 2017, **103**, 25–35.
11 Y. Xu, W. Zhu, T. Wang, L. Jin, T. Liu, X. Li, *et al.*, Low molecule weight fucoidan mitigates atherosclerosis in ApoE (-/-) mouse model through activating multiple signal pathway, *Carbohydr. Polym.*, 2019, **206**, 110–120.
12 G. M. Tomboc, J. Kim, Y. Wang, Y. Son, J. Li, J. Y. Kim, *et al.*, Hybrid layered double hydroxides as multifunctional nanomaterials for overall water splitting and supercapacitor applications, *J. Mater. Chem. A*, 2021, **9**(8), 4528–4557.
13 L. Nobs, F. Buchegger, R. Gurny and E. Allemann, *Polymeric Nanoporticles as Drug Delivery Systems*, VDI Ber, 2003, pp. 47–62.
14 R. J. Sengwa and S. Choudhary, Nonlinear enhancement of the dielectric properties of PVA-Al 2 O 3 nanocomposites, *Adv. Mater. Processes*, 2017, **2**(4), 280–287.
15 F. Ali and F. Maiz, Structural, optical and AFM characterization of PVA: La3+ polymer films, *Phys. B*, 2018, **530**, 19–23.
16 H. T. Ahmed and O. G. Abdullah, Preparation and composition optimization of PEO: MC polymer blend films to enhance electrical conductivity, *Polymers*, 2019, **11**(5), 853.
17 M. Wojdyr, Fityk: a general-purpose peak fitting program, *J. Appl. Crystallogr.*, 2010, **43**(5), 1126–1128.
18 M. A. Wikler, *Methods for Dilution Antimicrobial Susceptibility Tests for Bacteria that Grow Aerobically: Approved Standard*, CLSI, 2006, vol. 26.
19 G. D. Christensen, W. A. Simpson, A. L. Bisno and E. H. Beachey, Adherence of slime-producing strains of *Staphylococcus epidermidis* to smooth surfaces, *Infect. Immun.*, 1982, **37**(1), 318–326.
20 M. A. Ansari, H. M. Khan, A. A. Khan, S. S. Cameotra and R. Pal, Antibiofilm efficacy of silver nanoparticles against biofilm of extended spectrum β-lactamase isolates of *Escherichia coli* and *Klebsiella pneumoniae*, *Appl. Nanosci.*, 2014, **4**, 859–868.
21 A. I. El-Batal, G. S. El-Sayyad, N. E. Al-Hazmi and M. Gobara, Antibiofilm and antimicrobial activities of silver boron nanoparticles synthesized by PVP polymer and gamma rays against urinary tract pathogens, *J. Cluster Sci.*, 2019, **30**(4), 947–964.
22 F. Neese, The ORCA program system, *Wiley Interdiscip. Rev. Comput. Mol. Sci.*, 2012, **2**(1), 73–78.
23 F. Neese, Software update: the ORCA program system, version 4.0, *Wiley Interdiscip. Rev. Comput. Mol. Sci.*, 2018, **8**(1), e1327.

24 F. Neese, F. Wennmohs, U. Becker and C. Riplinger, The ORCA quantum chemistry program package, *J. Chem. Phys.*, 2020, **152**(22), 224108.
25 F. Neese, Software update: The ORCA program system—Version 5.0, *Wiley Interdiscip. Rev. Comput. Mol. Sci.*, 2022, **12**(5), e1606.
26 F. Neese, A Perspective on the Future of Quantum Chemical Software: The Example of the ORCA Program Package, *Faraday Discuss.*, 2024, **254**, 295–314.
27 R. Shafei, P. J. Strobel, P. J. Schmidt, D. Maganas, W. Schnick and F. Neese, A Combined Experimental and Computational Study on the Broadening Mechanism of the Luminescence in Narrow-Band Eu2+-Doped Phosphors, *J. Phys. Chem. C*, 2025, **129**, 1495–1505.
28 R. Shafei, D. Maganas, P. J. Strobel, P. J. Schmidt, W. Schnick and F. Neese, Electronic and optical properties of Eu2+-activated narrow-band phosphors for phosphor-converted light-emitting diode applications: Insights from a theoretical spectroscopy perspective, *J. Am. Chem. Soc.*, 2022, **144**(18), 8038–8053.
29 P. J. Stephens, F. J. Devlin, C. F. Chabalowski and M. J. Frisch, Ab initio calculation of vibrational absorption and circular dichroism spectra using density functional force fields, *J. Phys. Chem.*, 1994, **98**(45), 11623–11627.
30 A. D. Becke, Density-functional thermochemistry. III. The role of exact exchange, *J. Chem. Phys.*, 1993, **98**(7), 5648–5652.
31 C. Lee, W. Yang and R. G. Parr, Development of the Colle-Salvetti correlation-energy formula into a functional of the electron density, *Phys. Rev. B: Condens. Matter Mater. Phys.*, 1988, **37**(2), 785.
32 A. D. Becke, Density-functional exchange-energy approximation with correct asymptotic behavior, *Phys. Rev. A*, 1988, **38**(6), 3098–3100.
33 T. N. Truong and E. V. Stefanovich, A New Method for Incorporating Solvent Effect into the Classical, Ab-Initio Molecular-Orbital and Density-Functional Theory Frameworks for Arbitrary Shape Cavity, *Chem. Phys. Lett.*, 1995, **240**(4), 253–260.
34 R. Cammi and B. Mennucci, Linear response theory for the polarizable continuum model, *J. Chem. Phys.*, 1999, **110**(20), 9877–9886.
35 M. Garcia-Ratés and F. Neese, Effect of the Solute Cavity on the Solvation Energy and its Derivatives within the Framework of the Gaussian Charge Scheme, *J. Comput. Chem.*, 2020, **41**(9), 922–939.
36 R. K. Dongare, R. M. Tigote, M. P. Shinde, A. A. Skelton, S. P. Patole and S. N. Inamdar, DFT-based theoretical model for predicting the loading and release of pH-responsive paracetamol drug, *Mater. Today: Proc.*, 2023, DOI: **10.1016/j.matpr.2023.04.364**.
37 S. Nguyen and M. Hiorth, Advanced drug delivery systems for local treatment of the oral cavity, *Ther. Deliv.*, 2015, **6**(5), 595–608.
38 L. N. Ribeiro, A. C. Alcântara, G. H. Rodrigues da Silva, M. Franz-Montan, S. V. Nista, S. R. Castro, *et al.*, Advances in Hybrid Polymer-Based Materials for Sustained Drug Release, *Int. J. Polym. Sci.*, 2017, **2017**(1), 1231464.
39 J. Ghitman, R. Stan, G. Vlasceanu, E. Vasile and H. Iovu, Predicting the drug loading efficiency into hybrid nanocarriers based on PLGA-vegetable oil using molecular dynamic simulation approach and Flory-Huggins theory, *J. Drug Deliv. Sci. Technol.*, 2019, **53**, 101203.
40 M. Danaei, M. Dehghankhold, S. Ataei, F. Hasanzadeh Davarani, R. Javanmard, A. Dokhani, *et al.*, Impact of particle size and polydispersity index on the clinical applications of lipidic nanocarrier systems, *Pharmaceutics*, 2018, **10**(2), 57.
41 M. J. Masarudin, S. M. Cutts, B. J. Evison, D. R. Phillips and P. J. Pigram, Factors determining the stability, size distribution, and cellular accumulation of small, monodisperse chitosan nanoparticles as candidate vectors for anticancer drug delivery: application to the passive encapsulation of [14C]-doxorubicin, *Nanotechnol. Sci. Appl.*, 2015, 67–80.
42 M. S. Algahtani, M. Z. Ahmad and J. Ahmad, Investigation of factors influencing formation of nanoemulsion by spontaneous emulsification: impact on droplet size, polydispersity index, and stability, *Bioengineering*, 2022, **9**(8), 384.
43 R. Mahmoud, N. M. Kotb, Y. GadelHak, F. I. A. El-Ela, A. Z. Shehata, S. I. Othman, *et al.*, Investigation of ternary Zn–Co–Fe layered double hydroxide as a multifunctional 2D layered adsorbent for moxifloxacin and antifungal disinfection, *Sci. Rep.*, 2024, **14**(1), 806.
44 M. Vedanarayanan, C.-M. Chen and M. G. Sethuraman, Efficient hydrogen and oxygen evolution: dual-functional electrocatalyst of zinc iron layered double hydroxides and nickel cobalt sulfides on nickel foam for seawater splitting, *ACS Appl. Energy Mater.*, 2024, **7**(17), 7260–7271.
45 M. Yasaei, M. Khakbiz, A. Zamanian and E. Ghasemi, Synthesis and characterization of Zn/Al-LDH@ SiO2 nanohybrid: Intercalation and release behavior of vitamin C, *Mater. Sci. Eng., C*, 2019, **103**, 109816.
46 X. Zhu, C. Wei, N. Li and Z. Wang, The Modification of Dissolution Kinetics and Solubility of Lysozyme Crystals by Ionic Liquids, *J. Solut. Chem.*, 2024, **53**(6), 815–831.
47 L. Mursaleen, B. Noble, S. H. Y. Chan, S. Somavarapu and M. G. Zariwala, N-Acetylcysteine nanocarriers protect against oxidative stress in a cellular model of Parkinson's disease, *Antioxidants*, 2020, **9**(7), 600.
48 A. Zaher, M. Taha, A. A. Farghali and R. K. Mahmoud, Zn/Fe LDH as a clay-like adsorbent for the removal of oxytetracycline from water: combining experimental results and molecular simulations to understand the removal mechanism, *Environ. Sci. Pollut. Res.*, 2020, **27**, 12256–12269.
49 I. Lecomte, C. Henrist, M. Liégeois, F. Maseri, A. Rulmont and R. Cloots, (Micro)-structural comparison between geopolymers, alkali-activated slag cement and Portland cement, *J. Eur. Ceram. Soc.*, 2006, **26**(16), 3789–3797.
50 F. Puertas, M. Palacios, H. Manzano, J. Dolado, A. Rico and J. Rodríguez, A model for the CASH gel formed in alkali-

activated slag cements, *J. Eur. Ceram. Soc.*, 2011, **31**(12), 2043–2056.

51 N. Joshi, A. Pathak, R. Anupam, N. Jain, J. Singh and C. P. Upadhyaya, A rapid and efficient biosynthesis of metallic nanoparticles using aqueous extract of chia (*Salvia hispanica L.*) seeds, *BioNanoScience*, 2019, **9**(4), 893–902.

52 H. A. Hassanin and A. Taha, Sonochemical-assisted biogenic synthesis of theophrasite β-Ni (OH) 2 nanocluster using chia seeds extract: Characterization and anticancer activity, *Nanomaterials*, 2022, **12**(11), 1919.

53 M. Barakat, M. Anjum, R. Kumar, Z. Alafif, M. Oves and M. O. Ansari, Design of ternary Ni (OH) 2/graphene oxide/TiO2 nanocomposite for enhanced photocatalytic degradation of organic, microbial contaminants, and aerobic digestion of dairy wastewater, *J. Clean. Prod.*, 2020, **258**, 120588.

54 S. A. Moaty, A. Farghali and R. Khaled, Preparation, characterization and antimicrobial applications of Zn-Fe LDH against MRSA, *Mater. Sci. Eng., C*, 2016, **68**, 184–193.

55 H. Mohamed, R. Mahmoud, A. Abdelwahab, A. A. Farghali, F. I. A. El-Ela and A. E. Allah, Multifunctional ternary ZnMgFe LDH as an efficient adsorbent for ceftriaxone sodium and antimicrobial agent: sustainability of adsorption waste as a catalyst for methanol electro-oxidation, *RSC Adv.*, 2023, **13**(37), 26069–26088.

56 X. Yao, T. Du, J. Guo, W. Lv, B. Adhikari and J. Xu, Extraction and characterization of lysozyme from salted duck egg white, *Foods*, 2022, **11**(22), 3567.

57 R. Luo, X. Zhou, Y. Xiu and H. Wang, Preparation of hierarchically mesoporous bioactive glass and immobilization of lysozyme, *J. Sol-Gel Sci. Technol.*, 2018, **87**, 584–592.

58 M. D. Donohue and G. L. Aranovich, Classification of Gibbs adsorption isotherms, *Adv. Colloid Interface Sci.*, 1998, **76–77**, 137–152.

59 D. Steinberg and M. Friedman, Sustained-release drug delivery of antimicrobials in controlling of supragingival oral biofilms, *Expet Opin. Drug Deliv.*, 2017, **14**(4), 571–581.

60 D. Steinberg and M. Friedman, Dental drug-delivery devices: local and sustained-release applications, *Crit. Rev. Ther. Drug Carrier Syst.*, 1999, **16**(5), 36.

61 K. S. Kornman, Controlled-release local delivery antimicrobials in periodontics: Prospects for the future, *J. Periodontol.*, 1993, **64**, 782–791.

62 P. Costa and J. M. S. Lobo, Modeling and comparison of dissolution profiles, *Eur. J. Pharm. Sci.*, 2001, **13**(2), 123–133.

63 P. L. Ritger and N. A. Peppas, A simple equation for description of solute release II. Fickian and anomalous release from swellable devices, *J. Controlled Release*, 1987, **5**(1), 37–42.

64 T. Higuchi, Mechanism of sustained-action medication. Theoretical analysis of rate of release of solid drugs dispersed in solid matrices, *J. Pharmaceut. Sci.*, 1963, **52**(12), 1145–1149.

65 S. Sen, R. Samat, M. Jash, S. Ghosh, R. Roy, N. Mukherjee, *et al.*, Potential broad-spectrum antimicrobial, wound healing, and disinfectant cationic peptide crafted from snake venom, *J. Med. Chem.*, 2023, **66**(16), 11555–11572.

66 S. Sen, S. Ghosh, A. Jana, M. Jash, S. Ghosh, N. Mukherjee, *et al.*, Multi-faceted antimicrobial efficacy of a quinoline-derived bidentate copper (II) ligand complex and its hydrogel encapsulated formulation in methicillin-resistant *Staphylococcus aureus* inhibition and wound management, *ACS Appl. Bio Mater.*, 2024, **7**(6), 4142–4161.

67 S. Ghosh, S. Sen, M. Jash, S. Ghosh, A. Jana, R. Roy, *et al.*, Synergistic augmentation of beta-lactams: exploring quinoline-derived amphipathic small molecules as antimicrobial potentiators against methicillin-resistant *Staphylococcus aureus*, *ACS Infect. Dis.*, 2024, **10**(4), 1267–1285.

68 S. Motyka, B. Kusznierewicz, H. Ekiert, I. Korona-Głowniak and A. Szopa, Comparative analysis of metabolic variations, antioxidant profiles and antimicrobial activity of *Salvia hispanica* (Chia) seed, sprout, leaf, flower, root and herb extracts, *Molecules*, 2023, **28**(6), 2728.

69 A. M. Abdel-Aty, A. M. Elsayed, H. A. Salah, R. I. Bassuiny and S. A. Mohamed, Egyptian chia seeds (*Salvia hispanica L.*) during germination: Upgrading of phenolic profile, antioxidant, antibacterial properties and relevant enzymes activities, *Food Sci. Biotechnol.*, 2021, **30**, 723–734.

70 M. S. Coelho, R. A. M. Soares-Freitas, J. A. G. Arêas, E. A. Gandra and M. M. Salas-Mellado, Peptides from chia present antibacterial activity and inhibit cholesterol synthesis, *Plant Foods Hum. Nutr.*, 2018, **73**, 101–107.

71 N. P. Krishnappa, S. A. Basha, P. S. Negi and U. J. Prasada Rao, Phenolic acid composition, antioxidant and antimicrobial activities of green gram (*Vigna radiata*) exudate, husk, and germinated seed of different stages, *J. Food Process. Preserv.*, 2017, **41**(6), e13273.

72 N. Nagappan, K. Palaneeswaran, K. Kumarappan, R. Natarajan, R. Tajuddin and Y. Anusha, Antimicrobial efficacy of herbal and chlorhexidine mouthrinse against *Staphylococcus aureus*-an in vitro microbiological study, *J. Pharm. BioAllied Sci.*, 2022, **14**, S318–S322.

73 E. Al-Ani, D. Hill and K. Doudin, Chlorhexidine Mucoadhesive Buccal Tablets: The Impact of Formulation Design on Drug Delivery and Release Kinetics Using Conventional and Novel Dissolution Methods, *Pharmaceuticals*, 2021, **14**(6), 493.

74 L. D. de Carvalho, B. U. Peres, Y. Shen, M. Haapasalo, H. Maezono, A. P. Manso, *et al.*, Chlorhexidine-Containing Electrospun Polymeric Nanofibers for Dental Applications: An In Vitro Study, *Antibiotics*, 2023, **12**(9), 1414.

75 S.-Y. Han, J. Roh, Y.-S. Jung and K.-R. Kim, Evaluation of Antimicrobial Activity of Chlorhexidine-Containing Oral Gels Against Aspiration Pneumonia-Inducing Bacteria: An: In Vitro: Study, *Indian J. Dent. Res.*, 2022, **33**(1), 90–93.

76 J. J. Pucher and C. Daniel, The effects of chlorhexidine digluconate on human fibroblasts in vitro, *J. Periodontol.*, 1992, **63**(6), 526–532.

77 H. Babich, B. Wurzburger, Y. Rubin, M. Sinensky and L. Blau, An in vitro study on the cytotoxicity of chlorhexidine digluconate to human gingival cells, *Cell Biol. Toxicol.*, 1995, **11**, 79–88.

78 F. Cieplik, N. S. Jakubovics, W. Buchalla, T. Maisch, E. Hellwig and A. Al-Ahmad, Resistance toward chlorhexidine in oral bacteria–is there cause for concern?, *Front. Microbiol.*, 2019, **10**, 587.

79 H. G. M. Saleem, C. A. Seers, A. N. Sabri and E. C. Reynolds, Dental plaque bacteria with reduced susceptibility to chlorhexidine are multidrug resistant, *BMC Microbiol.*, 2016, **16**, 1–9.

80 A. A. Eweis, M. S. Ahmad, E. B. El Domany, M. Al-Zharani, M. Mubarak, Z. E Eldin, *et al.*, *Actinobacterium*-Mediated Green Synthesis of CuO/Zn–Al LDH Nanocomposite Using *Micromonospora* sp. ISP-2 27: A Synergistic Study that Enhances Antimicrobial Activity, *ACS Omega*, 2024, **9**(32), 34507–34529.

81 S. A. A. Abdel Aziz, Y. GadelHak, M. B. E. D. Mohamed and R. Mahmoud, Antimicrobial properties of promising Zn–Fe based layered double hydroxides for the disinfection of real dairy wastewater effluents, *Sci. Rep.*, 2023, **13**(1), 7601.

82 J. Awassa, S. Soulé, D. Cornu, C. Ruby and S. El-Kirat-Chatel, Understanding the role of surface interactions in the antibacterial activity of layered double hydroxide nanoparticles by atomic force microscopy, *Nanoscale*, 2022, **14**(29), 10335–10348.

83 M. E. Elkartehi, A. Zaher, A. Farghali, M. Ma, R. Mahmoud and N. Shehata, Antibacterial activities of layer double hydroxide nanocubes based on Zeolite templates and its high performance as a disinfectant, *Egypt. J. Chem.*, 2023, **66**(3), 265–270.

84 D. H. Wardhani, H. N. Ulya, A. Rahmawati, T. V. Sugiarto, A. C. Kumoro and N. Aryanti, Preparation of degraded alginate as a pH-dependent release matrix for spray-dried iron and its encapsulation performances, *Food Biosci.*, 2021, **41**, 101002.

85 N. V. Ayala-Núñez, H. H. Lara Villegas, L. del Carmen Ixtepan Turrent and C. Rodríguez Padilla, Silver nanoparticles toxicity and bactericidal effect against methicillin-resistant *Staphylococcus aureus*: nanoscale does matter, *Nanobiotechnology*, 2009, **5**, 2–9.

86 J. Yoon, J.-M. Park, S.-K. Jung, K.-Y. Kim, Y.-H. Kim and J. Min, Characterization of antimicrobial activity of the lysosomes isolated from *Saccharomyces cerevisiae*, *Curr. Microbiol.*, 2009, **59**, 48–52.

87 A. J. McBain, R. G. Ledder, L. E. Moore, C. E. Catrenich and P. Gilbert, Effects of quaternary-ammonium-based formulations on bacterial community dynamics and antimicrobial susceptibility, *Appl. Environ. Microbiol.*, 2004, **70**(6), 3449–3456.

88 W. Mendling, E. R. Weissenbacher, S. Gerber, V. Prasauskas and P. Grob, Use of locally delivered dequalinium chloride in the treatment of vaginal infections: a review, *Arch. Gynecol. Obstet.*, 2016, **293**, 469–484.

89 T. Zaidieh, J. R. Smith, K. E. Ball and Q. An, ROS as a novel indicator to predict anticancer drug efficacy, *BMC Cancer*, 2019, **19**, 1–14.

90 S. Motyka, H. Ekiert and A. Szopa, Skład chemiczny, aktywność biologiczna i zastosowanie nasion chia (*Salviae hispanicae semen*), *Farm. Pol.*, 2021, **77**(11), 651–661.

91 S. Motyka, K. Koc, H. Ekiert, E. Blicharska, K. Czarnek and A. Szopa, The current state of knowledge on *Salvia hispanica* and *Salviae hispanicae semen* (chia seeds), *Molecules*, 2022, **27**(4), 1207–1227.

92 A. Duda-Chodak, T. Tarko, P. Satora and P. Sroka, Interaction of dietary compounds, especially polyphenols, with the intestinal microbiota: a review, *Eur. J. Nutr.*, 2015, **54**, 325–341.

93 K. Belosludtsev, N. Belosludtseva, K. Tenkov, V. Sharapov, E. Kosareva and M. Dubinin, Effect of dequalinium on respiration and the inner membrane permeability of rat liver mitochondria, *Biochem. (Mosc), Suppl. Ser. A Membr. Cell Biol.*, 2018, **12**, 121–127.

94 S. B. Park, S. B. White, C. S. Steadman, T. Pechan, O. Pechanova, H. J. Clemente, *et al.*, Silver-coated magnetic nanocomposites induce growth inhibition and protein changes in foodborne bacteria, *Sci. Rep.*, 2019, **9**(1), 17499.

95 S. T. Omara, I. Abd El-Moez and M. Mohamed, Antibacterial effect of *Origanum majorana* L.(marjoram) and *Rosmarinus officinalis* L. (rosemary) essential oils on food borne pathogens isolated from raw minced meat in Egypt, *Glob. Vet.*, 2014, **13**(6), 1056–1064.

96 G. P. Andrews, T. P. Laverty and D. S. Jones, Mucoadhesive polymeric platforms for controlled drug delivery, *Eur. J. Pharm. Biopharm.*, 2009, **71**(3), 505–518.

97 X. He, X. Xie, H. Xu, J. Liu, B. Li and Q. Zhang, Promoted removal of phosphate by layered double hydroxides combined with bacteria: Application of novel carriers in biofilm reactor, *Bioresour. Technol.*, 2022, **349**, 126879.

98 B. Ballarin, A. Mignani, F. Mogavero, S. Gabbanini and M. Morigi, Hybrid material based on ZnAl hydrotalcite and silver nanoparticles for deodorant formulation, *Appl. Clay Sci.*, 2015, **114**, 303–308.

99 R. Mahmoud, Z. E. Eldin, A. Khalifa, A. A. A. Anwar, Y. GadelHak, S. I. Othman, *et al.*, Antifungal and antibacterial investigation of quinary Zr Al Fe Co Ni layered double hydroxide and its Al Fe Co Ni quaternary and Fe Co Ni tertiary roots, *RSC Adv.*, 2024, **14**(21), 14815–14834.

100 G. Francius, E. André, S. Soulé, C. Merlin and C. Carteret, Layered Double Hydroxides (LDH) as nanocarriers for antimicrobial chemotherapy: From formulation to targeted applications, *Mater. Chem. Phys.*, 2023, **293**, 126965.

101 N. J. Laible and G. Germaine, Bactericidal activity of human lysozyme, muramidase-inactive lysozyme, and cationic polypeptides against *Streptococcus sanguis* and *Streptococcus faecalis*: inhibition by chitin oligosaccharides, *Infect. Immun.*, 1985, **48**(3), 720–728.

102 S. A. Ragland and A. K. Criss, From bacterial killing to immune modulation: Recent insights into the functions of lysozyme, *PLoS Pathog.*, 2017, **13**(9), e1006512.
103 M. Zhao, M. Huang and Z. Li, Exploring the therapeutic potential of recombinant human lysozyme: a review on wound management system with antibacterial, *Front. Bioeng. Biotechnol.*, 2023, **11**, 1292149.
104 V. Kirstilä, M. Lenander-Lumikari, E. Söderling and J. Tenovuo, Effects of oral hygiene products containing lactoperoxidase, lysozyme, and lactoferrin on the composition of whole saliva and on subjective oral symptoms in patients with xerostomia, *Acta Odontol. Scand.*, 1996, **54**(6), 391–397.